Supporting Information for

"Estimates of aseismic slip associated with small earthquakes near San Juan Bautista, CA"

J. C. Hawthorne[1], M. Simons[2], J.-P. Ampuero[2]

[1]School of Earth and Environment, University of Leeds

[2]Seismological Laboratory, Division of Geological and Planetary Sciences, California Institute of Technology

Contents

Additional Supporting Information (Files uploaded separately)

1. Table of newly identified reset pulses (SJT-reset-pulses)
2. Table of intervals with large noise (SJT-noisy-intervals)

S1 Predicted Strain Calculations

We calculate the predicted strain from the seismic moment assuming horizontal slip on a fault in a half space. The fault strikes 135° and dips 80° SW. This strike and dip are within 2° of the best-fitting plane to the local seismicity. The half space has shear modulus 30 GPa and Poisson's ratio 0.25.

We illustrate the spatial pattern of strain in Figure S1, which shows the strains that would be produced at the strainmeter by an earthquake at the specified location. To simplify the plot, we have normalized the distances by the earthquake depth, and the amplitude of strain is normalized by the earthquake potency over depth^3.

Most of the earthquakes plot along a line in the depth-normalized space. The ε_{E-N} strain (Figure S1b) has a maximum along this line. The large values and slow variation of the Green's function along this line make ε_{E-N} more robust for modeling. The ε_{E+N} and ε_{2EN} strains (Figure S1a and c) have nodal planes close to the fault's surface projection. The near-zero os-

Corresponding author: J. C. Hawthorne, J.C.Hawthorne@leeds.ac.uk

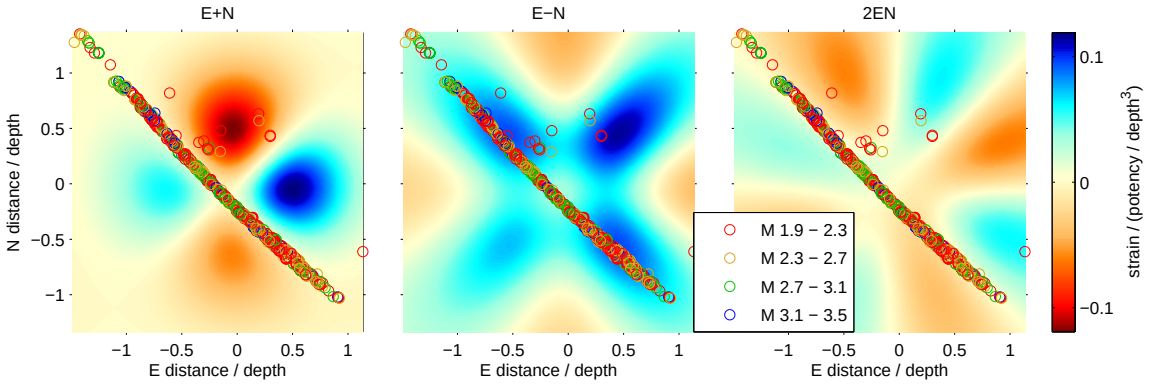

Figure S1. Strain as a function of earthquake location. Note that the pattern would be reversed if strain were plotted as a function of observation location. The earthquakes mostly lie along a line in this depth-normalized plot. They fall near maxima for ε_{E-N} but near nodal planes for ε_{E+N} and ε_{2EN}.

cillating values are difficult to predict and model. The quick variation is part of the reason that many of the predictions in Figure 4a have the wrong sign. We do not use ε_{E+N} or ε_{2EN} when we average over small earthquakes in section 5.

S2 Initial Strain Processing

Before stacking the strain signal associated with earthquakes, we remove four non-tectonic signals: reset pulses, a 3-hour instrumental signal, tides, an and atmospheric response. Reset pulses are roughly 3-hour-long signals are generated by the instrument at 10-day intervals. The pulses that occurred after 2006 were already removed by J. Langbein and others at the USGS. We identify pulses that occurred before 2006 and remove the data during those periods. The times of the additional pulses are listed in the supplementary material.

We also visually identify time intervals with outliers in the strain data. These are likely related to instrumental errors or to noise close to the borehole. The intervals are listed in the supplementary material.

A second, and somewhat more mysterious, instrumental effect is a repeating signal with a period of 3 hours. This signal displays no change in form, amplitude, or timing through the 30-year record. The consistency suggests that this signal is an instrumental artifact. The 3-hour period suggests that it may be related to the data transmission, which occurs every 3 hours. The consistency of this signal also makes it easy to remove. We isolate it by stacking the strain record in 3-hour increments and subtract it from the strain record.

The third, and largest, signal we remove is the tidal variation. In order isolate this signal, we highpass filter the data to exclude periods longer than 3 days. We exclude data within 1-2 days of nearby creep events and large earthquakes and intervals unusually large variance. We fit a set of 17 sinusoids to the remaining data. The sinusoids have the periods of 26.8684, 25.8193, 24.8332, 24.0659, 24.0000, 23.9345, 23.0985, 22.3061, 13.1272, 12.8718, 12.6583, 12.4206, 12.1916, 12.0000, 11.9672, 11.7545, and 8.2804 hours. The cosine and sine components at each period are allowed to vary linearly within 5-year segments. This linear variation accounts for small changes in coupling and for the roughly 5% variation in the inferred amplitudes due to the 18.6-year lunar nodal precession.

The fourth and final signal we remove is the change in strain in response to atmospheric pressure. We compare the observed strain with atmospheric pressure variations derived from ECMWF atmospheric reanalysis model [*Dee et al.*, 2011]. All three components of strain are correlated with atmospheric pressure variations. However, for ε_{E+N} and ε_{E-N}, the maximum correlation lags the atmospheric pressure changes by about 15 and 6 hours, respectively. This lag may be a physical effect. Spatial variations in pore pressure can cause a delayed change in strain at the borehole [e.g., *Roeloffs*, 2010]. The temporal resolution of the atmospheric model could also play a role. The ECMWF model is estimated only every 6 hours and on a 200-km grid [*Dee et al.*, 2011]. However, it is unclear why the lag would vary among the three components.

Since we do not understand the delay, and since most energy in the atmospheric pressure changes are at periods of a few days or longer, we choose to ignore the lag in correlation. We compute a single in-phase correction for atmospheric pressure for the entire time series and remove it from the data. In any case, the atmospheric pressure correction is small. Omitting it does not change our results and increases the error bars only marginally.

S3 Discrepancies in Observed and Predicted Coseismic Strain

In section 4 and Figure 4 we noted that the coseismic strain in well-resolved $M > 3$ earthquakes often differs from our predictions. The ε_{E+N} and ε_{2EN} offsets often have different signs, and even the better-resolved ε_{E-N} offsets are a factor of 2 to 8 larger than the predictions (see Figure 7a). Stacks of ε_{E-N} in small earthquakes from section 6 give similarly large coseismic offsets: 3 to 5 times the predictions (Figure 7a).

S3.1 Possible Sources of Error

A significant portion of these discrepancies likely results from uncertainties in our elastic modeling, which neglects spatially dependent earth structure. The ε_{E+N} and ε_{2EN} offsets are especially sensitive to this error because the strainmeter lies near a nodal plane in their Green's function (Figure S1a and c). The nearly nodal location also makes the predicted ε_{E+N} and ε_{2EN} offsets sensitive to error in the modeled strike and dip.

To better constrain the error allowed by uncertainty in the fault plane, we compute the synthetic strains for six of the earthquake locations considered in section 4. For each location, we randomly select 500 strikes, dips, and rakes from 10-degree bands centered on a strike of 135°, a dip of 80° SW, and a rake of 180° (right-lateral). The strains predicted for these varying fault orientations are shown in Figure S2. For ε_{E+N} and ε_{2EN}, the predicted strains can be both positive and negative even with this small range of geometry changes. This strong variation explains why the observed coseismic ε_{E+N} and ε_{2EN} steps often differ in sign from the predictions. Small variations in fault orientation can to some extent explain why the ε_{E+N} and ε_{2EN} offsets typically have amplitudes larger-than-predicted amplitudes, as the predicted strain per moment is smaller for the preferred fault plane (vertical lines in Figure S2) than for planes with slightly different orientations (histograms in Figure S2).

However, the orientations seem unlikely to explain some of the exceptionally large discrepancies. Even for the best-resolved ε_{E-N}, offsets for $M < 3$ earthquakes sometimes differ from the predictions by a factor of 100. The large scatter suggests that for at least some earthquakes, the assumed seismic moments or Green's functions are dramatically wrong. On the other hand, the tendency of the observed strains to increase relative to the predictions as the earthquake magnitude decreases suggests that we may be preferentially selecting outliers for $M < 3$ earthquakes. We plot offsets in Figures 4 only if the ratio of the observed postseismic to coseismic strain is well resolved, and the ratio would not be well-resolved if the strains were closer to the predictions. This outlier selection should not occur in the stacks of $M < 3.5$ earthquakes, as the stacks average over all available earthquakes.

In the stacks (Figure 7), the average coseismic ε_{E-N} is 3 to 5 times the predictions, similar to values obtained for individual $M > 3.5$ earthquakes (Figure 4a). This systematic offset is too large to be explained by the errors in fault plane orientation explored in Figure S2. Part of the systematic overprediction could come from spatial variation in the elastic structure. Qualitatively, one expects larger surface strains if the elastic moduli are significantly reduced

near the surface. The P-wave velocity model of *Lin et al.* [2010] includes a roughly 1 km/s P-wave velocity increase between 1 and 4 km depth in the San Juan Bautista area. For standard velocity-density scaling relationships [*Brocher*, 2005], such a P-wave velocity change would lead to a roughly 50% change in the shear modulus in this depth range. If such a shear modulus change with depth is uniform over a large area, it could lead to observed coseismic strains being a few tens of percent larger than the predictions for a homogeneous half space (*Cattin et al.* [1999]; *Segall* [2010], section 5.5.3).

The predicted coseismic strains could also change significantly if the elastic structure varies horizontally, especially if it varies on length scales of a few kilometers, comparable to the earthquake depths. In studies of fault scale locking distributions, low-modulus fault zones and changes in stiffness across the fault have been inferred to enhance near-fault strain rates by a factor of 1.5 to 2 *Chen and Freymueller* [2002]; *Schmalzle et al.* [2006]; *Jolivet et al.* [2009]. Seismic observations consistently reveal a 0.5 to 1.5 km/s P-wave speed increase from the southwest to the northeast side of the San Andreas Fault [e.g. *Eberhart-Phillips and Michael*, 1993; *Thurber et al.*, 2006; *Lin et al.*, 2010]. It is not obvious how this asymmetry would affect the strain at SJT. The strainmeter is located in sandstone near the surface projection of the seismicity, but 1.5 km southwest of the surface trace of the San Andreas [*Gladwin et al.*, 1987].

In fact, elastic strain calculations are complicated further by the strainmeter calibration. The observed strain amplitudes were calibrated to the known tidal strains. The tidal strains occur in the same elastic medium and with the same boundary conditions as the earthquake induced strains, so one might expect that the tidal calibration would accommodate small-scale variations in elastic structure [*Hart et al.*, 1996]. However, the tidal strains near San Juan Bautista are dominated by the body tides, which have wavelengths within a factor of a few of the Earth's circumference. It is possible that kilometer-scale heterogeneity in the elastic structure would affect these long-wavelength strains differently than it would affect the coseismic strains, which decay over several km.

The strainmeter calibration itself could introduce some additional error. *Langbein* [2010] and *Langbein* [2015] estimated several tens of percent error in the tidal calibration of instruments near Parkfield, CA in the San Francisco Bay area, respectively. We may expect similar errors for SJB, located near San Juan Bautista, CA, at an intermediate distance from the coast. Such calibration errors may be accentuated for the ε_{E+N} and ε_{2EN} strains, which have Green's functions that vary quickly in space near the strainmeter.

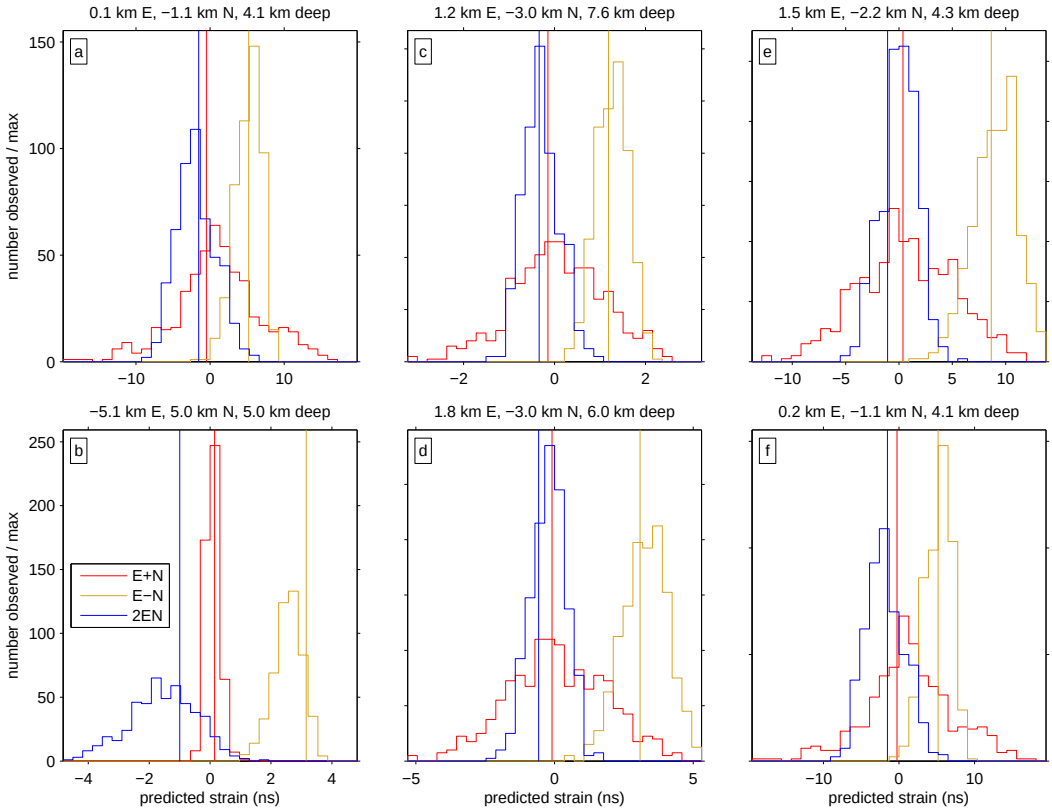

Figure S2. Distribution of predicted strains obtained by varying the strike, dip, and rake in uniform 10-degree areas around the best estimates. Strains are computed for each of six earthquake locations, one for each panel. All earthquakes are assumed to be M_W 3.5. The earthquake location relative to the strainmeter is indicated by the title. Color indicates the strain component of interest. Vertical lines mark the predicted strains for the default slip orientation.

Error in the predicted strain could also be due to errors in the seismic moment. Here we use moments estimated from the NCSN catalog magnitudes using the calibration of *Hawthorne et al.* [accepted], which was created specifically for the 20-km region around San Juan Bautista. The moment is calculated as a function of the catalog duration magnitudes M:

$$M_0 = 10^{1.1(M-3.5)} 2.2 \times 10^{14} \text{ N m}. \quad (1)$$

With this calibration, typical errors in the relative moments of two earthquakes are around a factor of 1.5. But there is an additional error of similar order in the overall calibration: in the average moment of all the earthquakes used. Given these uncertainties, errors in the seismic moment could easily contribute about half of a factor of 3 discrepancy between the predicted and observed strain offsets, but it is not clear if they can explain the entire difference.

Finally, discrepancies between the predicted and observed coseismic offsets could arise if there is significant postseismic slip in the first 20 minutes after the earthquakes, as was suggested by large strain in the first five minutes after the 2004 M 6.0 Parkfield earthquake [*Borcherdt et al.*, 2006]. For instance, if postseismic slip accumulates logarithmically with time starting 1 s after the earthquake [as in e.g., *Marone et al.*, 1991; *Perfettini and Avouac*, 2004; *Savage and Langbein*, 2008], the moment accumulation within 20 minutes will equal the moment accumulated between 20 minutes and 1.5 days. Such early postseismic slip is difficult to examine in individual earthquakes because strain is sampled at 18-minute intervals. However, in sections 6.2 and S8 we see that stacked data from smaller earthquakes suggest only minor early postseismic moment.

To summarize, there are a several sources of uncertainties that could contribute a few tens of percent of the factor of 3 to 5 discrepancy between the predicted and observed coseismic strain. These include uncertainties in the fault orientation, the strain Green's functions, the strainmeter calibration, the seismic moment scaling, and the early postseismic slip. Of these possibilities, errors in the local Green's function and seismic moment scaling seem most likely to make larger contributions.

S3.2 Consistency With Static Strain Scaling

Given the difficulty in resolving the discrepancy in the predicted and observed coseismic strain, it would seem reasonable to consider alternative sources of strain. For instance, *Barbour et al.* [2015] found that coseismic strain offsets in southern California were proportional

to the dynamic shaking. Here we explore the scaling of the observed coseismic offsets with the predicted dynamic and static strains.

In Figure S3 we plot the amplitude of the coseismic (20-minute) offset for a number of earthquakes on all three components. The static strains in a full space are expected to scale as the earthquake moment divided by the earthquake-strainmeter distance cubed [*Lay and Wallace*, 1995], so in Figure S3a we plot the observed offsets against moment over distance cubed. The black line shows the static strain amplitude predicted for this geometrical spreading, assuming a density of 3 g/cm^3 and a shear wave velocity of 3 km/s, but ignoring the free surface, the component dependence, and the spatially dependent radiation pattern. As was seen for the individual earthquakes in Figure 4, the observed offsets are larger than the predicted strain, and there is large scatter. However, the offsets do come close to following a one-to-one line with the predicted static scaling (dashed-dotted line in Figure S3a).

In contrast, the observed offsets do not follow a one-to-one scaling with the predicted maximum dynamic strain, shown on the x-axis of Figure S3b. The maximum dynamic strain is expected to scale as the maximum moment rate divided by distance squared [*Lay and Wallace*, 1995]. To obtain a rough moment rate for each earthquake, we estimate the earthquake radius assuming a 3-MPa stress drop [*Brune*, 1970], and then assume the duration is equal to the radius divided by the shear wave speed. The moment rate is then the earthquake moment divided by the duration. This moment rate allows us to predict the maximum dynamic strain, which, as expected, does not accurately predict the 20-minute static strain offsets (Figure S3b).

On the other hand, if dynamic effects induce static strain in some other way, as the result of shaking the borehole [*Barbour et al.*, 2015], it may not be the dynamic strain that is most important. In Figure S3c we plot the observed offsets against the expected scaling factor for maximum dynamic displacement: moment rate divided by distance. A one-to-one scaling from predicted dynamic displacement matches the observed static offsets less well than the predicted static scaling.

To further verify that the static strain scaling is a reasonable approximation to the data, we identify the moments and distances of earthquakes that cause significant static strain. In Figure S4, earthquakes with a 20-minute offset that is significant at the 90% level are plotted in yellow or red. The strain-inducing earthquakes are well delimited by a line of constant moment over distance cubed (M_0/r^3)—the expected scaling of static strain.

For comparison, we also plot lines of constant M_0/r^2 and M_0/r in Figure S4. These scalings might be the relevant criteria for strain caused by shaking if strain is triggered by deformation at a specified period longer than the earthquake—for instance, if a pore pressure seal can be broken by shaking at periods of 10 seconds but not at shorter periods. The strain and displacement variations at a specified period are expected to scale as M_0/r^2 and M_0/r, respectively. However, these scalings do not accurately delimit the earthquakes that cause deformation. The inaccurate scalings suggest that dynamic deformations at timescales longer than the earthquakes do not determine the coseismic offsets.

With these observations of the coseismic offsets, we cannot rule out a dynamic effect on the mostly sub-second earthquake timescales. However, given the consistent plausibility of the static strain scaling, coupled with the consistent ratio of postseismic to coseismic strain, as well as the variations in sign of the observed offsets, which are consistent with the static predictions but difficult to explain through shaking, it seems simplest and most plausible to interpret the data in terms of static strain induced by coseismic slip, and to attribute the factor of 3 to 5 discrepancy between the predicted and observed coseismic strains mostly to errors in the assumed elastic structure, which could contribute to systematic errors in both strain predictions and seismic moment estimates.

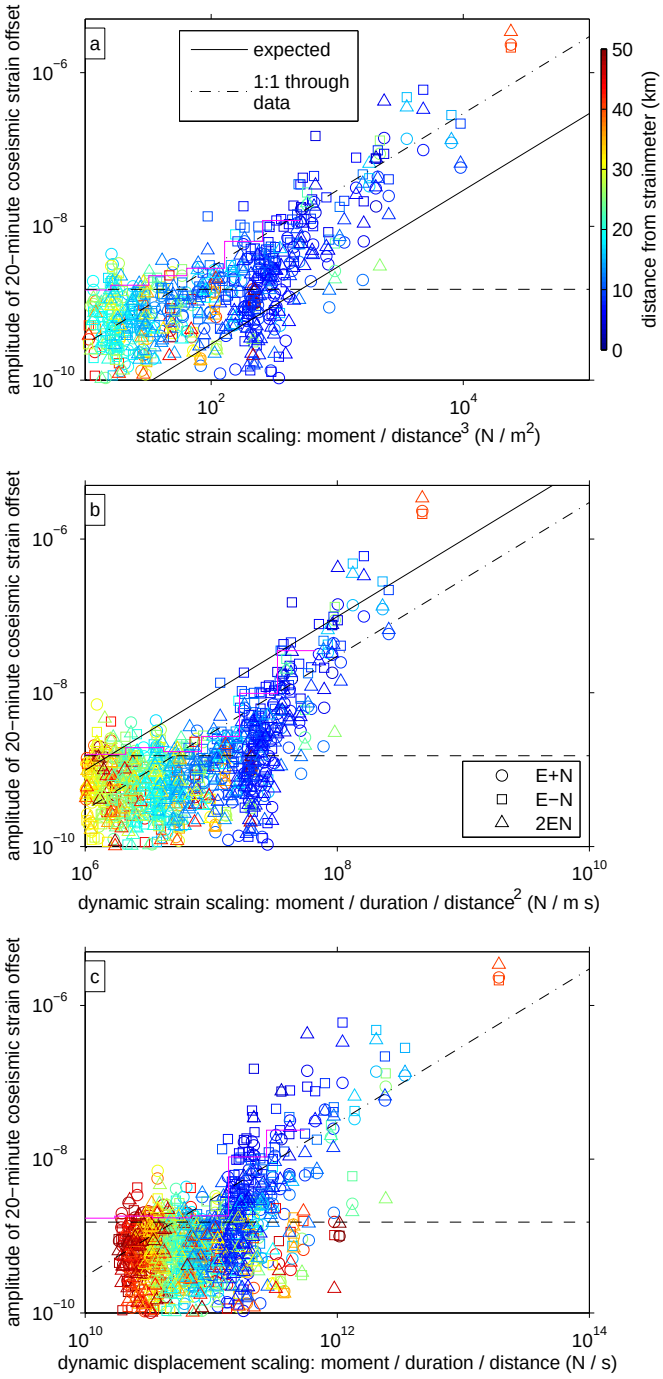

Figure S3. Observed coseismic (20-minute) strain offsets as a function of the predicted scaling factors for static strain (panel a), dynamic strain (panel b), and dynamic displacement (panel c). Color indicates distance from the strainmeter, and symbol indicates the observing component. In panels a and b, black lines shows the predicted static and dynamic strain amplitudes, respectively, adjusting only for geometric spreading. Dashed-dotted lines show one-to-one scalings between the observations and the scaling factors that pass through the data. Horizontal dashed lines indicates a 90% uncertainty in the 20-minute offsets. Magenta lines mark the 95th percentile of the coseismic offsets, which matches the uncertainty when the predicted strain is small.

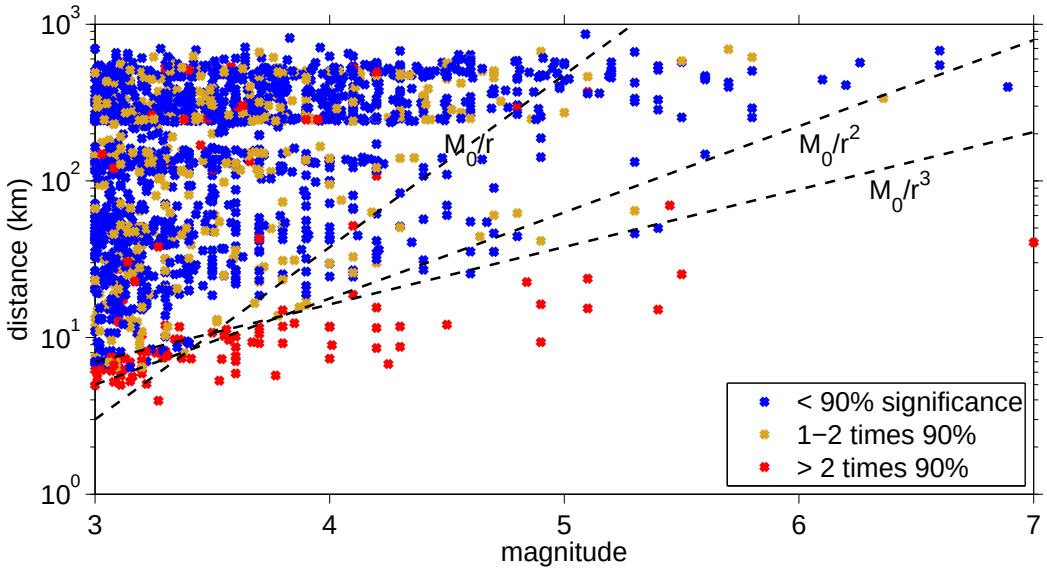

Figure S4. Distances and magnitudes of earthquake with measured 20-minute coseismic offsets, colored by the significance of that offset. Dashed curves show lines of constant moment M_0 over distance r cubed, M_0/r^2, and M_0/r, respectively. The highly significant observations are well-delimited by a line of constant M_0/r^3, as would be expected if the observed offsets represent static elastic strain.

S4 Strain in Large Earthquakes

In section 4 we analyzed the strain in large nearby earthquakes. Figures S5 to S23 show the corrected strain time series from those events.

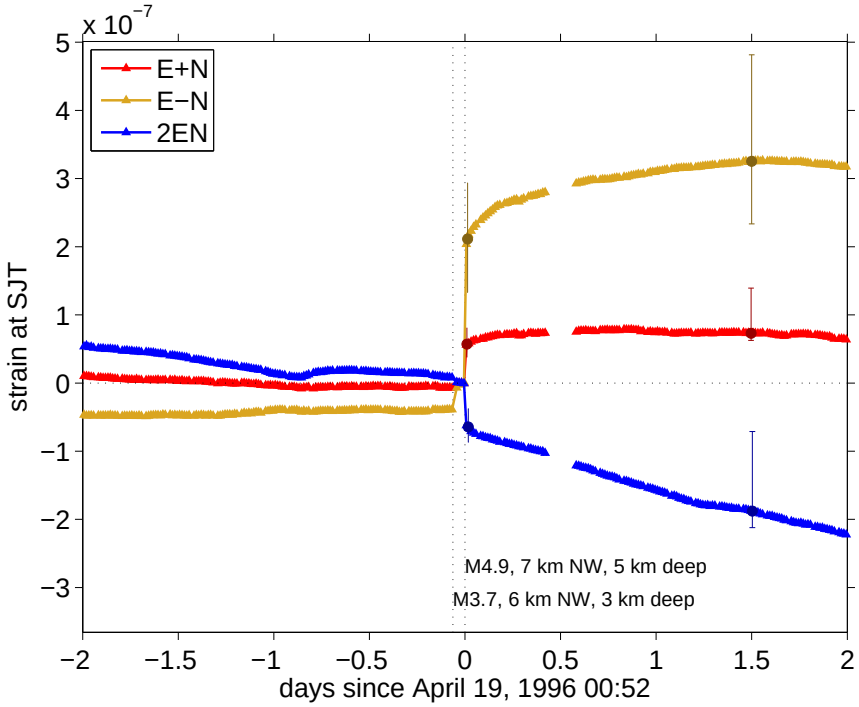

Figure S5. Strain associated with a nearby M 4.9 earthquake. Components are indexed by color. The filled circles and error bars indicate the best-fitting offsets and the 90% confidence interval, computed as described in section 4.

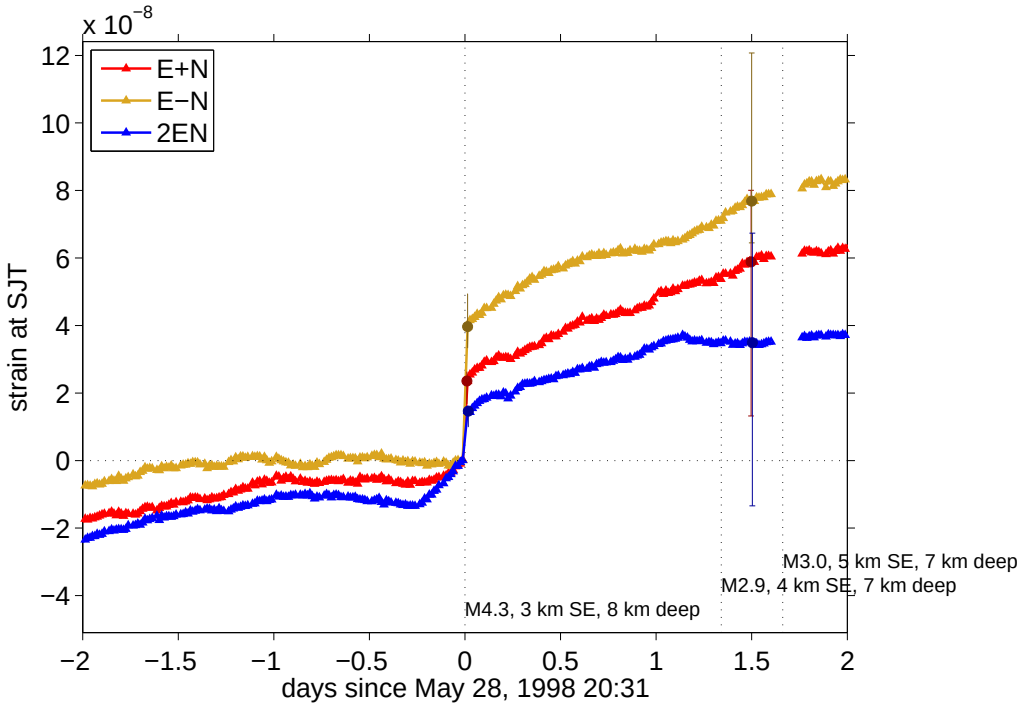

Figure S6. Strain associated with a nearby M 4.3 earthquake.

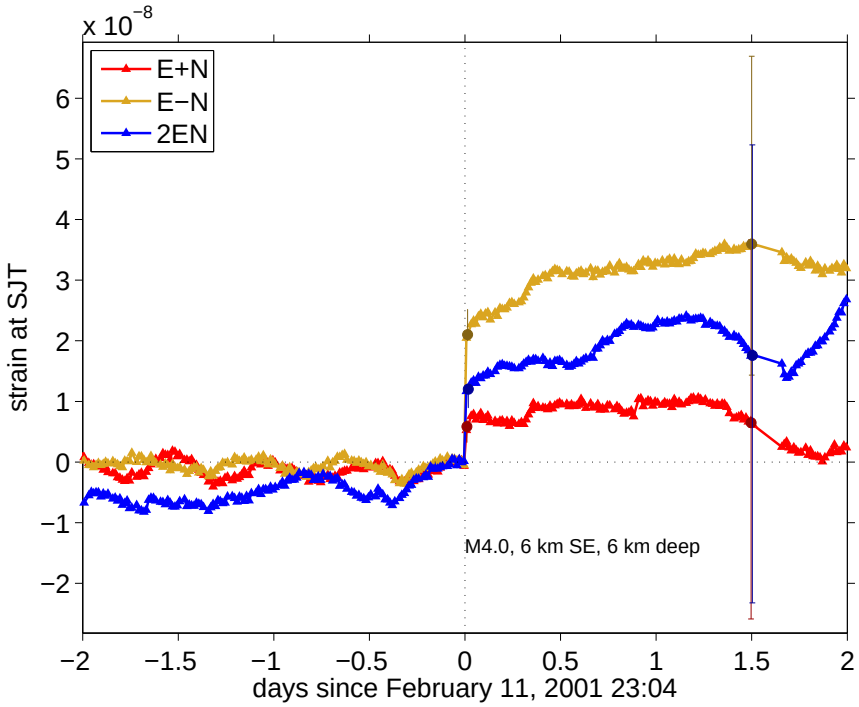

Figure S7. Strain associated with a nearby M 4.0 earthquake.

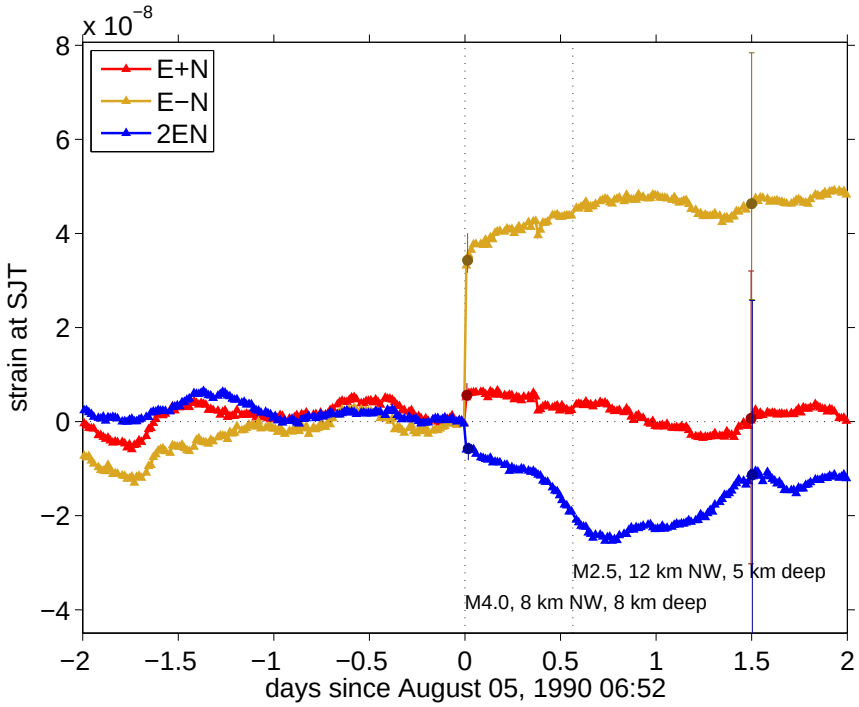

Figure S8. Strain associated with a nearby M 4.0 earthquake.

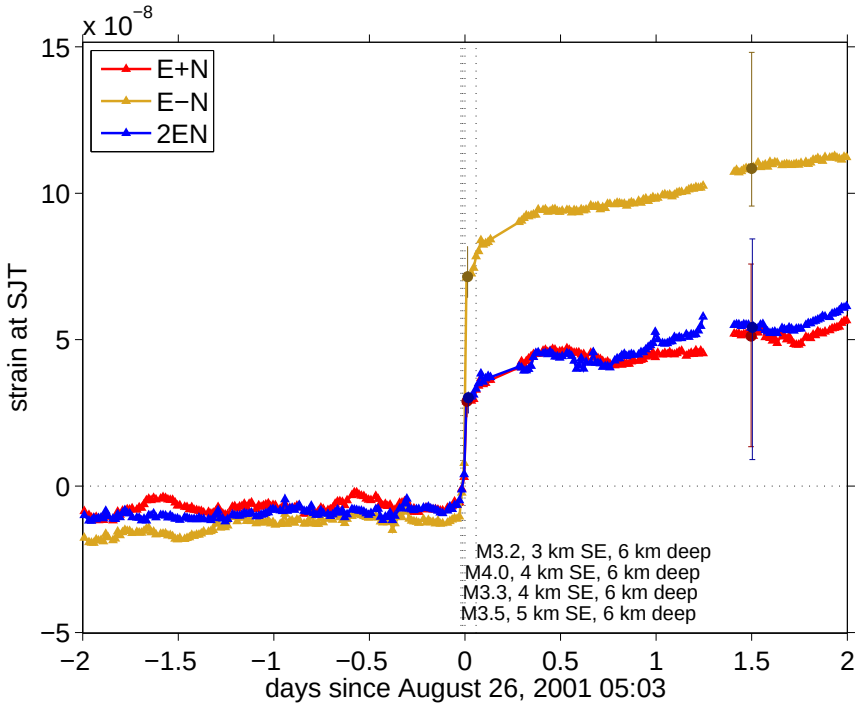

Figure S9. Strain associated with a nearby M 4.0 earthquake.

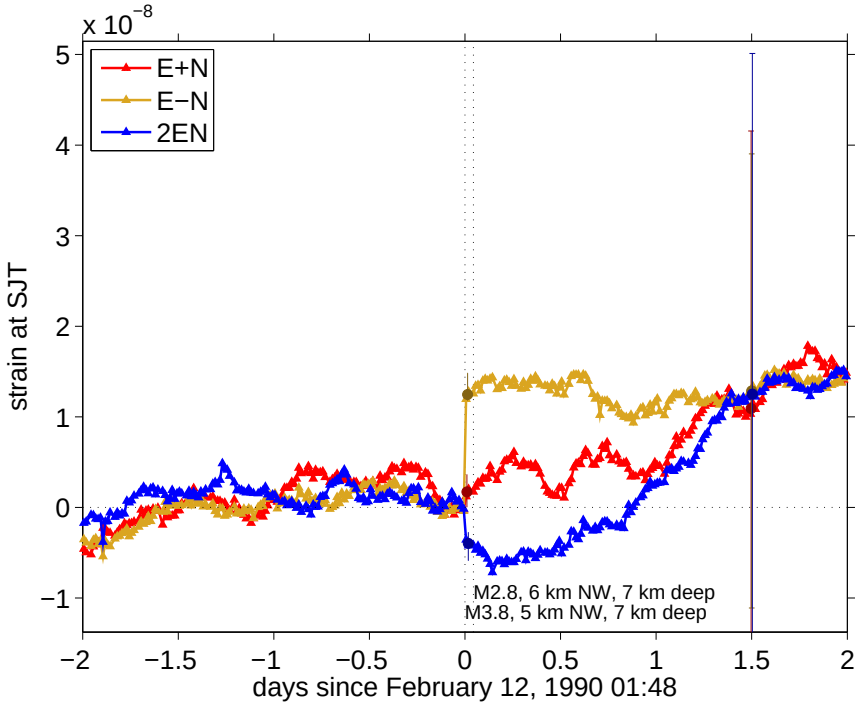

Figure S10. Strain associated with a nearby M 3.8 earthquake.

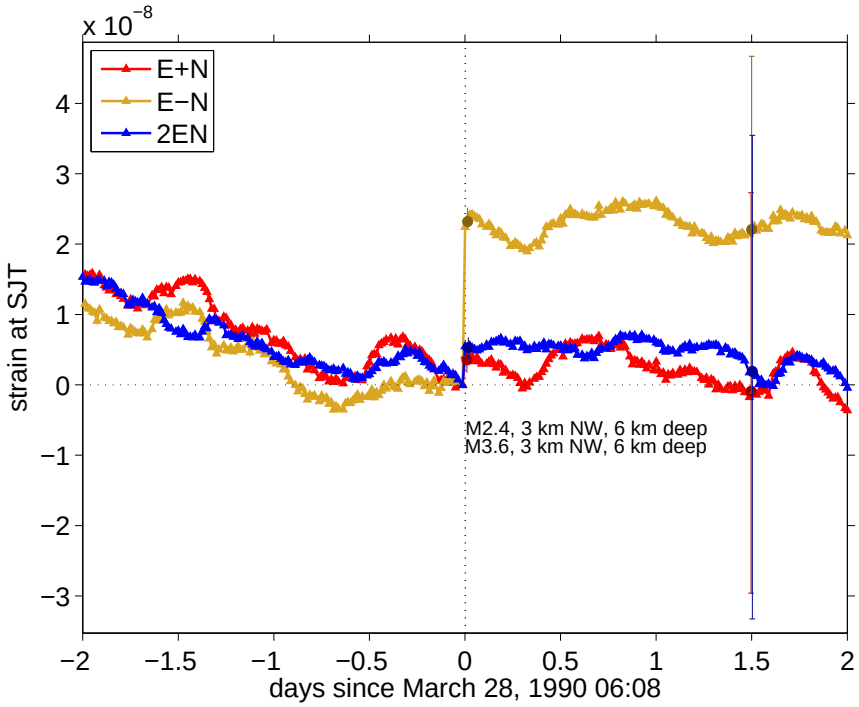

Figure S11. Strain associated with a nearby M 3.6 earthquake.

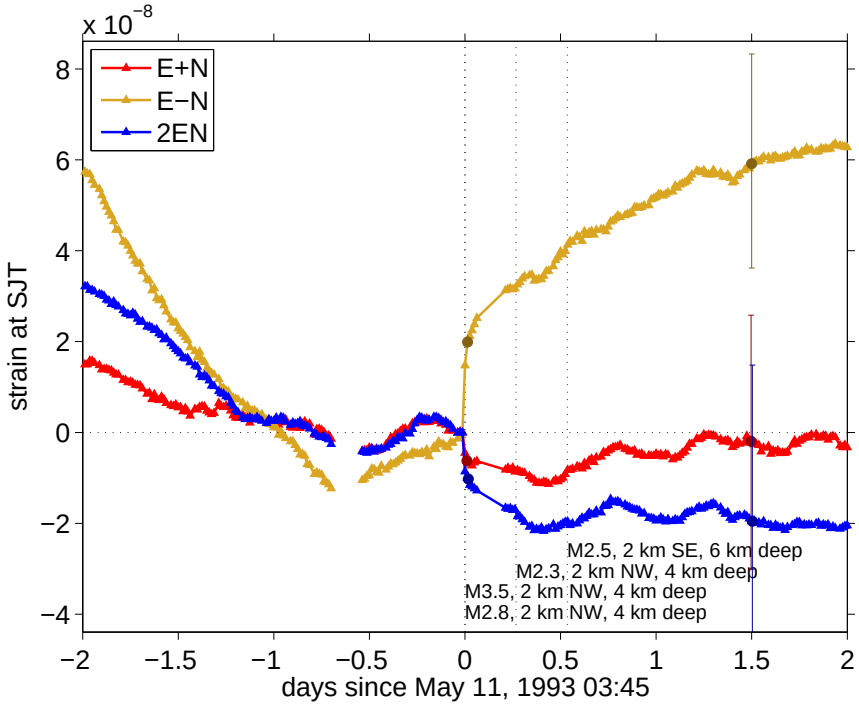

Figure S12. Strain associated with a nearby M 3.5 earthquake.

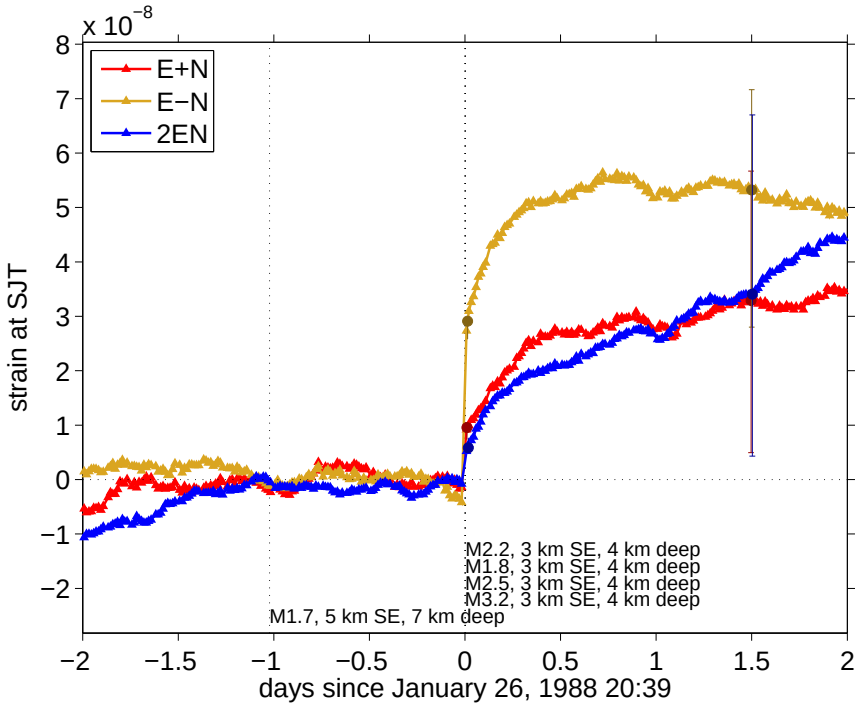

Figure S13. Strain associated with a nearby M 3.2 earthquake.

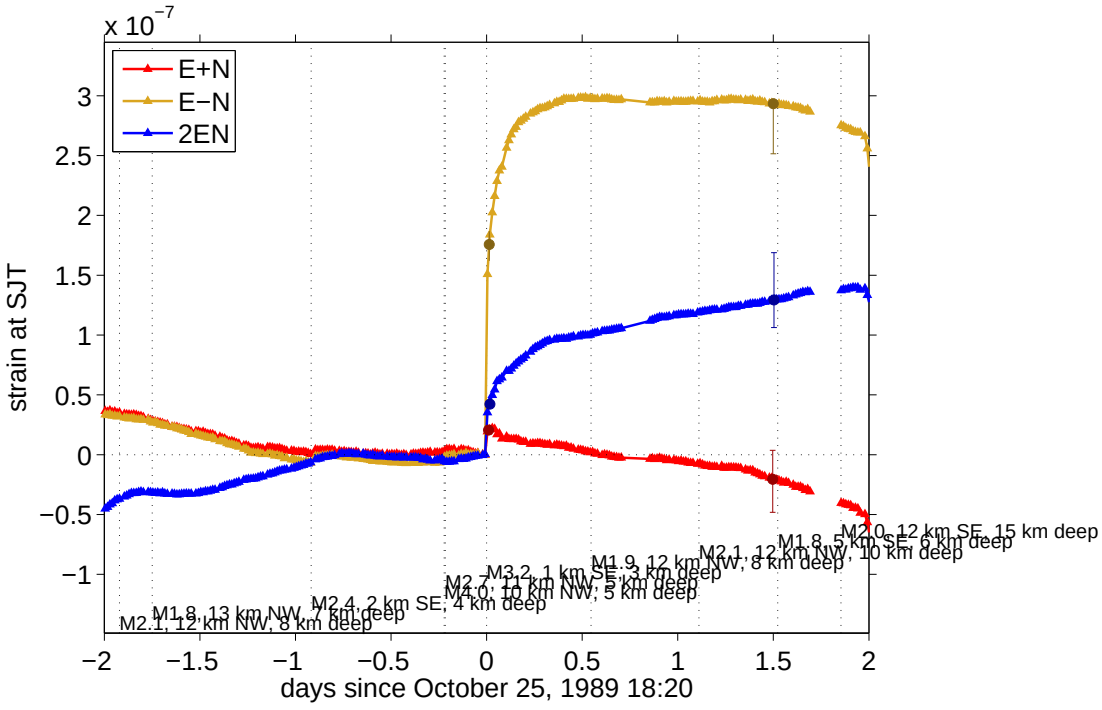

Figure S14. Strain associated with a nearby M 3.2 earthquake.

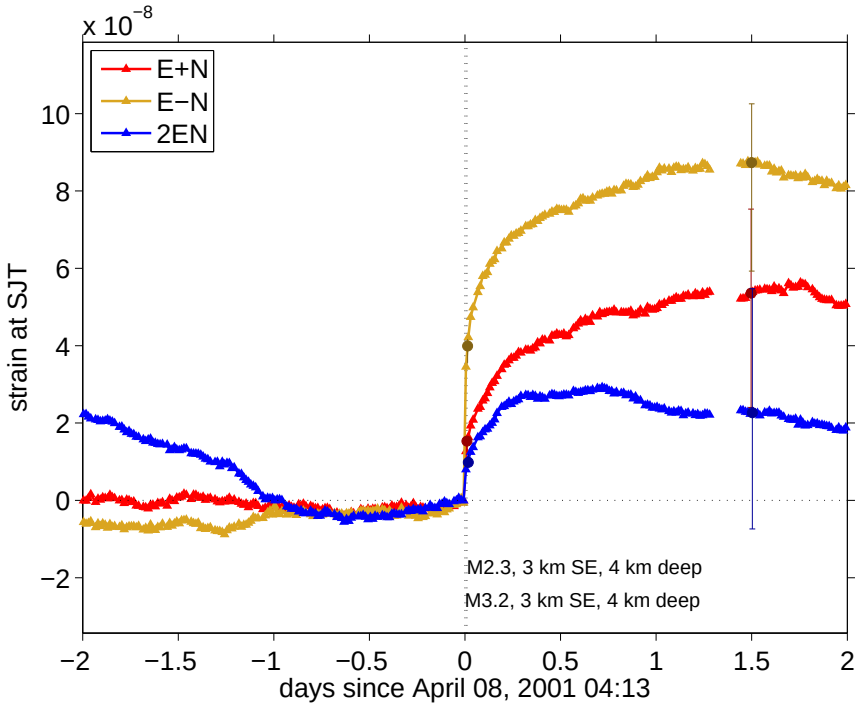

Figure S15. Strain associated with a nearby M 3.2 earthquake.

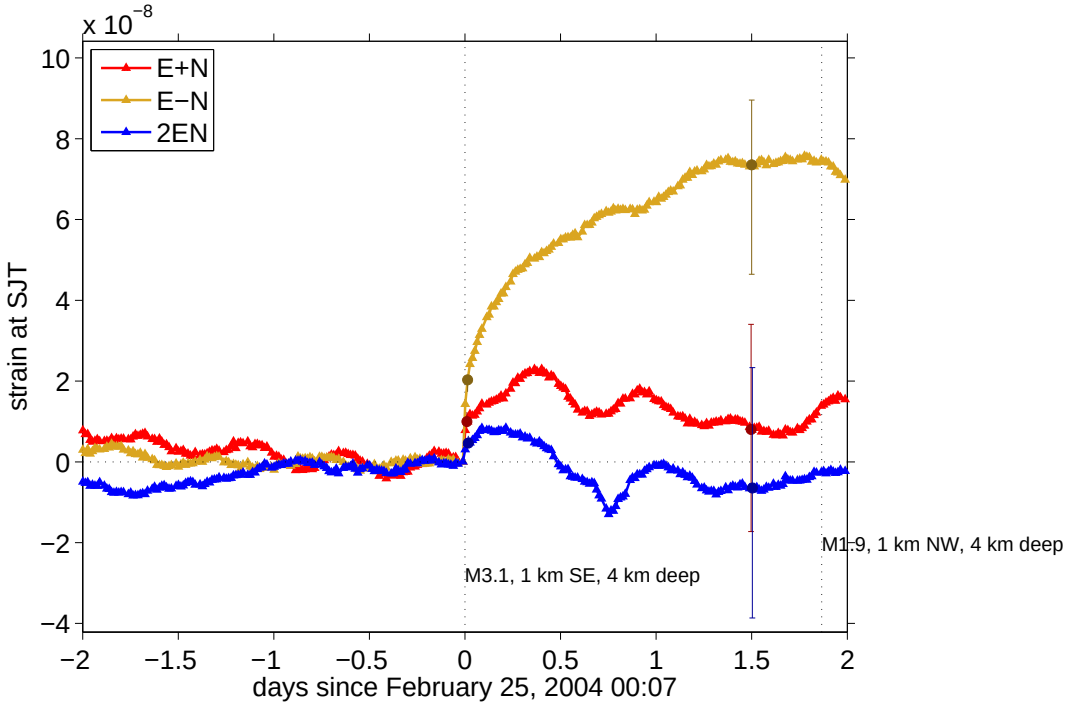

Figure S16. Strain associated with a nearby M 3.1 earthquake.

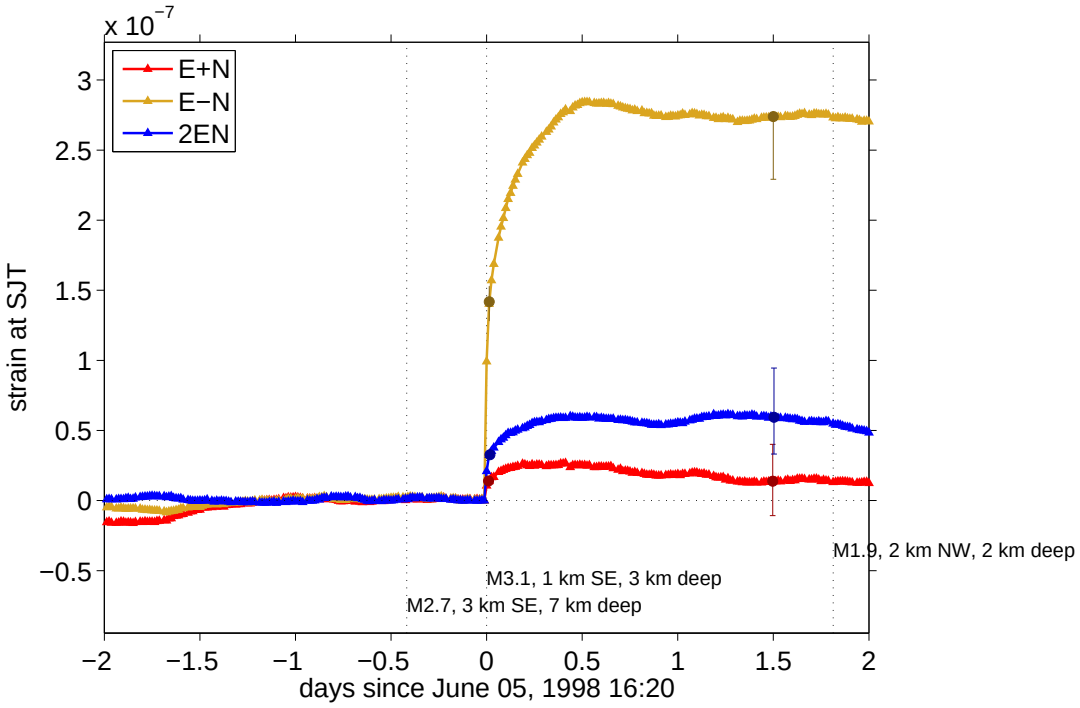

Figure S17. Strain associated with a nearby M 3.1 earthquake.

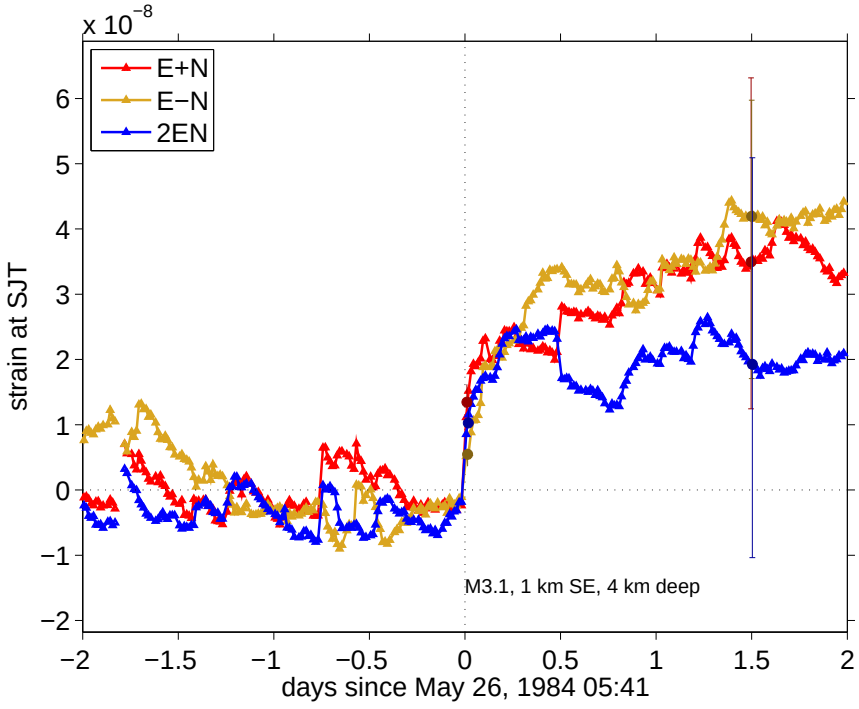

Figure S18. Strain associated with a nearby M 3.1 earthquake.

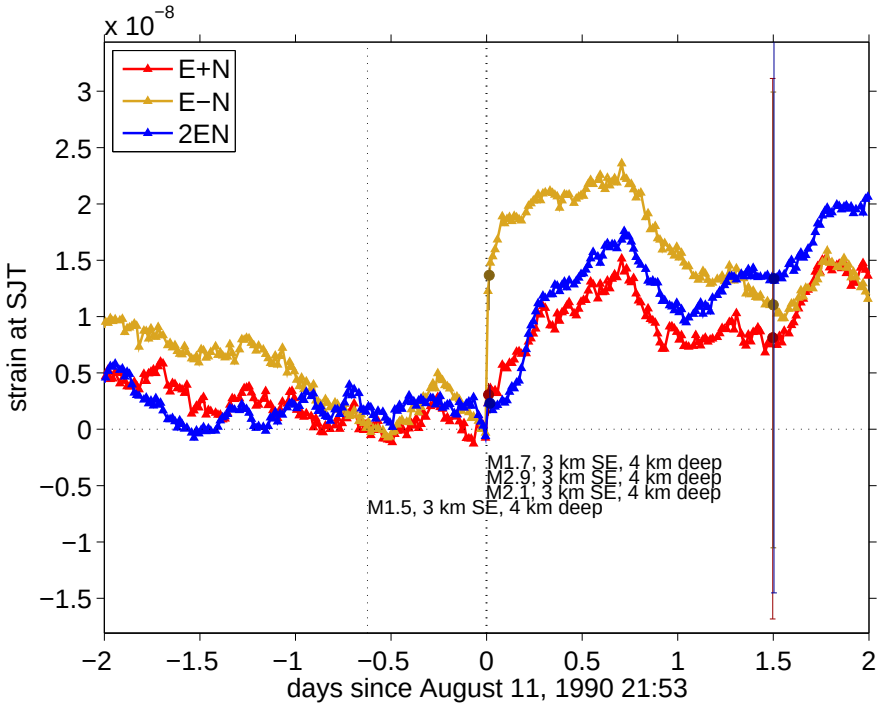

Figure S19. Strain associated with a nearby M 2.9 earthquake.

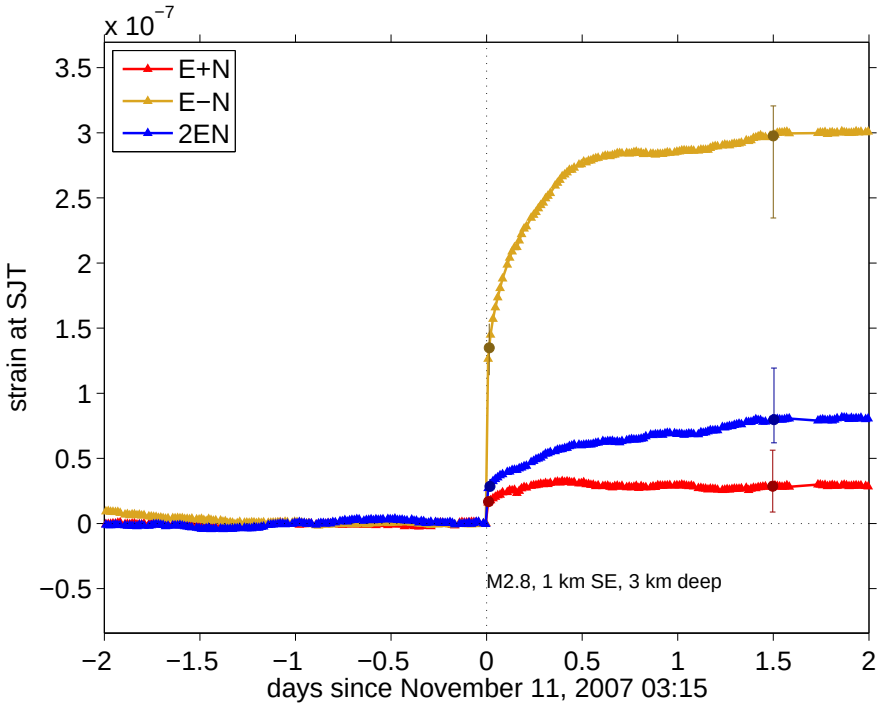

Figure S20. Strain associated with a nearby M 2.8 earthquake.

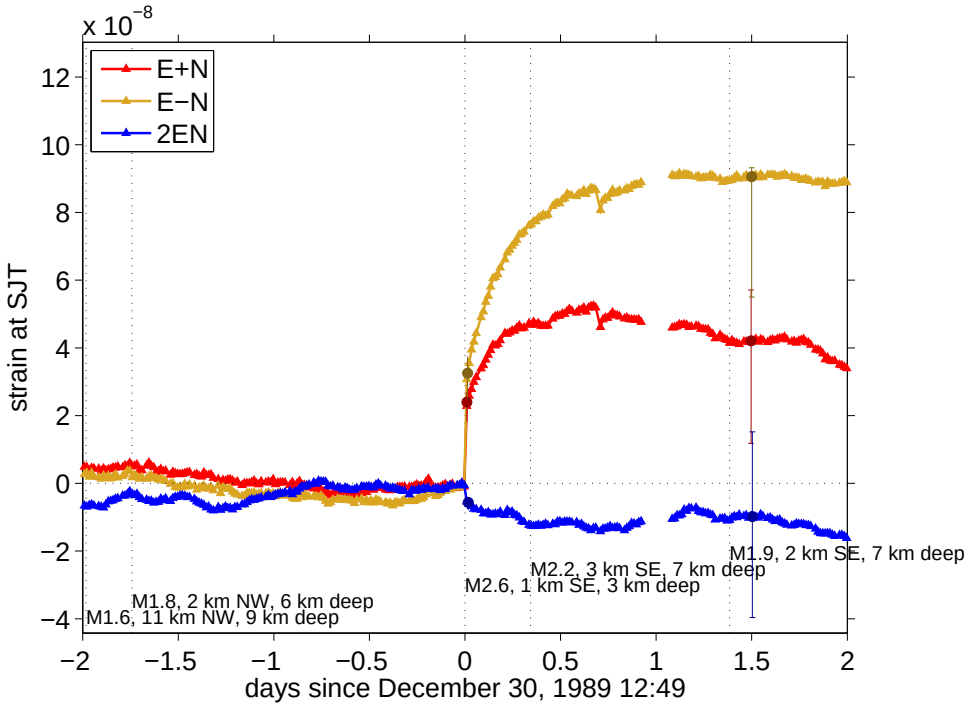

Figure S21. Strain associated with a nearby M 2.6 earthquake.

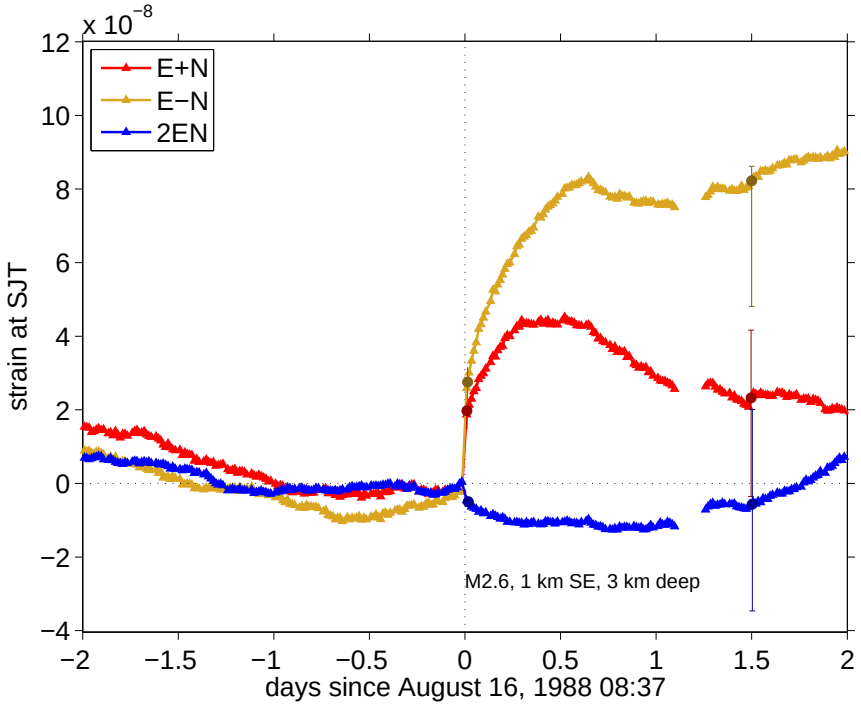

Figure S22. Strain associated with a nearby M 2.6 earthquake.

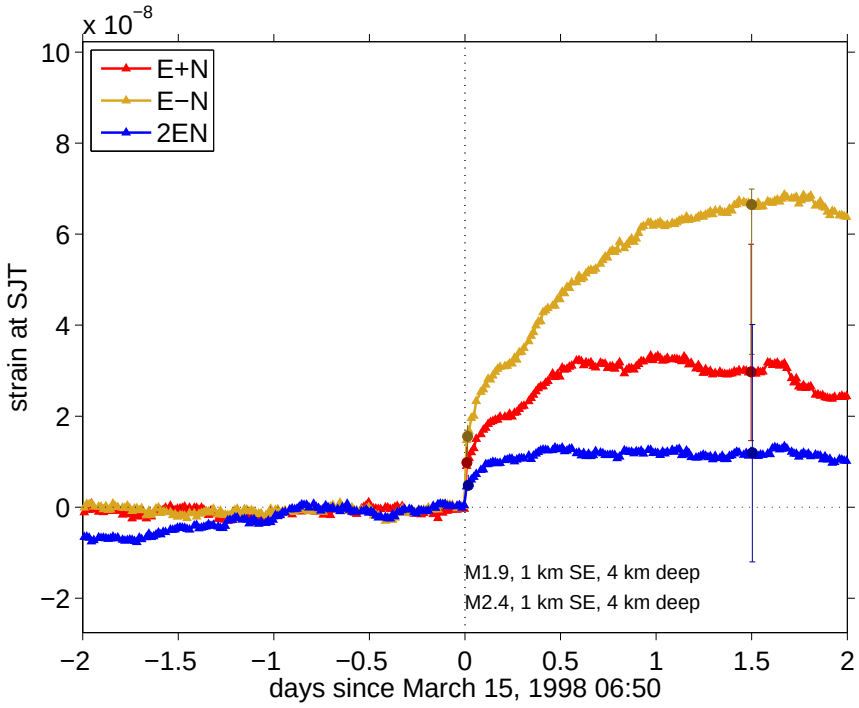

Figure S23. Strain associated with a nearby M 2.4 earthquake.

S5 Earthquakes Included in the Stack

As noted in section 5, we stack data from 1098 of the approximately 1500 $M \geq 1.9$ earthquakes that occurred within 10 km of strainmeter SJT and listed in the NCSN catalog. The 1500 earthquakes initially considered were relocated by *Waldhauser and Schaff* [2008] and *Waldhauser* [2009]. They occur within 3 km of the seismicity-lineated fault, between 3 and 10 km depth, and within 10 km of the station along strike (Figure 2).

We consider strain from $1.9 \leq M < 3.5$ earthquakes. To avoid mapping strain due to larger earthquakes into our results, we exclude all strain data within 2 days of any $M \geq 3.5$ earthquake within 20 km. We also exclude data within 5 days of creep events identified at nearby creepmeter XSJ [as in *Gladwin et al.*, 1994]. After eliminating these sections of the data, we refine the set of earthquakes in the stack. We throw away events that are poorly constrained by the data: that have no strain observations within 0.1 days of the earthquake time. We also exclude earthquakes whose predicted strain changes are smaller than 10^{-2} times the median predicted strain change. These earthquakes provide little information and their signals can be more easily biased.

The strain data could also be biased by $M < 3.5$ earthquakes that are too far from the fault to be included in our list. To alleviate this bias, we compute the magnitude of the expected strain for all nearby earthquakes that occur within 12 hours of an included event. We compare the summed strain of excluded earthquakes with the summed strain of included earthquakes in any magnitude group. We identify the excluded earthquakes that make the summed excluded strain larger than the strain in any magnitude group. We throw away any strain data within 0.5 days of those earthquakes. We then refine the included earthquakes to reflect the remaining data and repeat the process until the summed strain of excluded events is smaller then the strain in any bin. This selection results in 1098 earthquakes that are little affected by known biases. 518 are $1.9 \leq M < 2.3$, 287 are $2.3 \leq M < 2.7$, 229 are $2.7 \leq M < 3.1$, and 64 are $3.1 \leq M < 3.5$.

S6 Noise Model

The noise model $\mathbf{C}$ used when inverting for the normalized strain time series (equation (4)) is constructed from the spectra of the strain data. To estimate $\mathbf{C}$, we remove known non-tectonic signals and high-pass filter with a corner period of 20 days. We divide the data into overlapping 20-day segments, eliminate segments with especially large standard deviation, and com-

pute the spectra of the remaining segments with a multitaper approach [e.g., *Percival and Walden*, 1993]. These power spectra $\hat{C}(\text{frequency})$ are an estimate of the Fourier transform of the noise covariance $C(\Delta t)$. Here $C(\Delta t)$ is the covariance between spurious signals at times separated by Δt [e.g., *Langbein and Johnson*, 1997; *Langbein*, 2004]. Note that when we obtain $C(\Delta t)$, we use a corner period of 20 days rather than the 10-day corner period used for the forward model (equation (4)). The change in filtering downweights long-period noise so that the misfit is dominated by the short periods we are interested in.

S7 Division Into Segments

In order to solve for the normalized strain time series $\mathbf{f}$ while accounting for the noise model, we rewrite equation (4) and solve

$$\mathbf{C}^{-1/2}\mathbf{F}\mathbf{d} = \mathbf{C}^{-1/2}\mathbf{F}\mathbf{G}_e\mathbf{f}. \tag{2}$$

Here $\mathbf{C}^{-1/2}$ is a square root of the inverse of $\mathbf{C}$. However, $\mathbf{C}$ has nearly 10^6 values along each dimension because strain was recorded roughly every 18 minutes for 30 years. Computing the inverse of C would require a large computation. Much of this computation can be avoided by exploiting the structure of the noise. Since the data have been highpass filtered, $C(\Delta t)$ tends to zero for times separated by more than 10 days. We divide the data into 20-day-long segments, overlapping by 10 days. We assume that the noise covariance is zero for data points in different segments. Equation (4) then becomes

$$\begin{bmatrix} \mathbf{C}_1^{-1/2} & 0 & ... & 0 \\ 0 & \mathbf{C}_2^{-1/2} & ... & 0 \\ ... & ... & ... & ... \\ 0 & 0 & ... & \mathbf{C}_{N_s}^{-1/2} \end{bmatrix} \begin{bmatrix} (\mathbf{F}\mathbf{d})_1 \\ (\mathbf{F}\mathbf{d})_2 \\ ... \\ (\mathbf{F}\mathbf{d})_{N_s} \end{bmatrix} = \begin{bmatrix} \mathbf{C}_1^{-1/2} & 0 & ... & 0 \\ 0 & \mathbf{C}_2^{-1/2} & ... & 0 \\ ... & ... & ... & ... \\ 0 & 0 & ... & \mathbf{C}_{N_s}^{-1/2} \end{bmatrix} \begin{bmatrix} (\mathbf{F}\mathbf{G}_e)_1 \\ (\mathbf{F}\mathbf{G}_e)_2 \\ ... \\ (\mathbf{F}\mathbf{G}_e)_{N_s} \end{bmatrix} \mathbf{f}. \tag{3}$$

$\mathbf{C}_i$, $(\mathbf{F}\mathbf{d})_i$, and $(\mathbf{F}\mathbf{G}_e)_i$ are the noise covariance, filtered data, and filtered forward model for segment i. The block diagonal structure of the noise matrix allows us to solve equation (3) quickly but still retain a reasonable approximation of the temporal covariance. Changing the segment length to 10 days or to 40 days changes the results within our estimated errors.

S8 Postseismic Strain With Time

In section 6.2 we focused on the coseismic (20-minute) and total (1.5-day) strain offsets. Histograms of these offsets are shown in Figure S24a, f, and k. Also shown are offsets from 4 other intervals within the postseismic period.

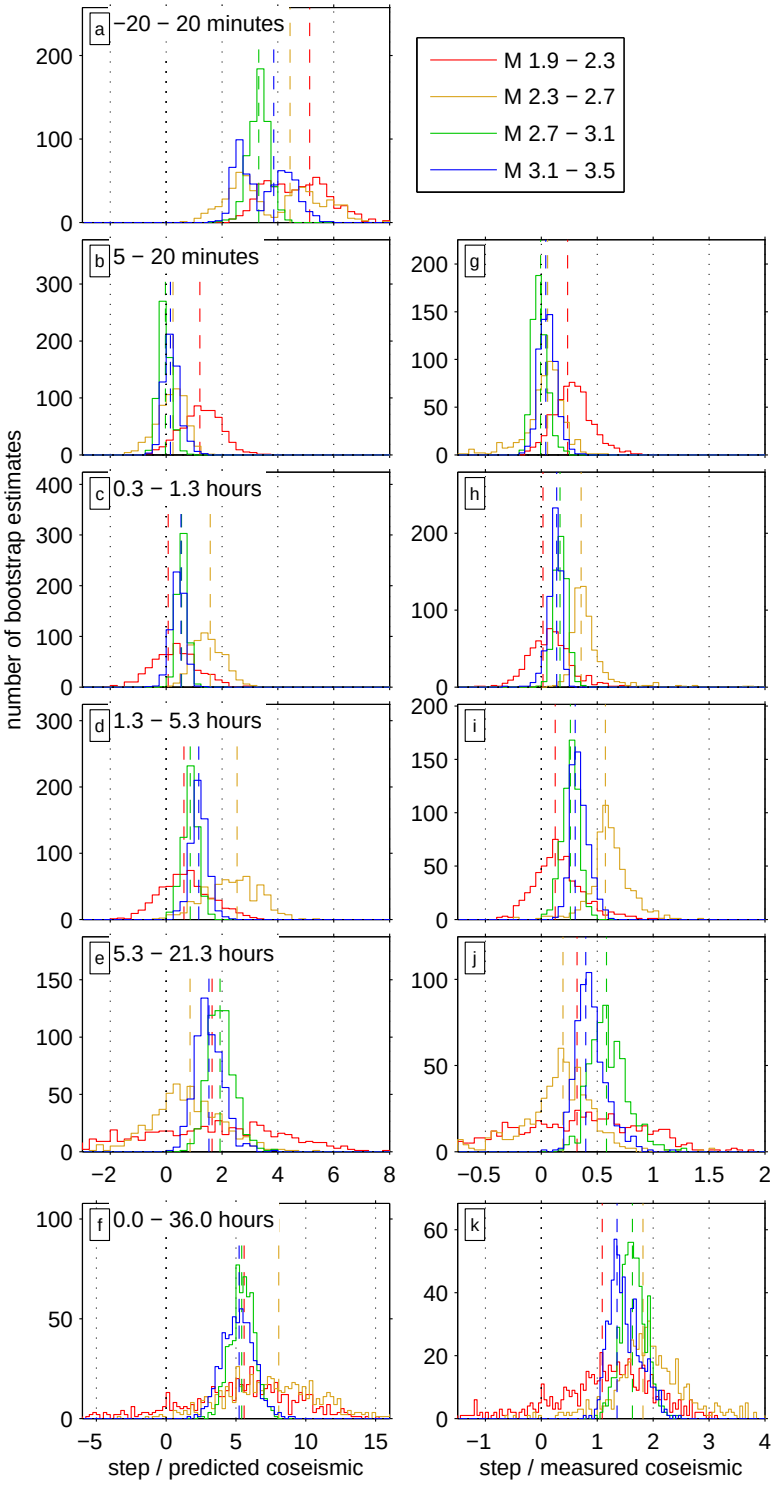

Figure S24. Histograms: distribution of strain offsets obtained from bootstrapping. Vertical dashed lines: best-fitting strain offsets. In the first column, the offsets are normalized by the predicted coseismic strain. In the second column, they are normalized by the observed coseismic strain. Color indicates the magnitude bin considered. The time range of the offsets is indicated by the text in the upper left hand corner of each row. The coseismic (20-minute, first row) and total (1.5-day, bottom row) offsets are also plotted against magnitude in Figure 7.

Of particular interest is the early postseismic strain accumulation: before 20 minutes, where we define the coseismic step. Many of the coseismic (20-minute) strain steps estimated in sections 4 and 6 are 2-6 times the predictions from the seismic moments. It is possible that some of the "extra" strain could be accumulating in the 20 minutes after the earthquake. For individual earthquakes, we must include that 20-minute interval in the coseismic step because of the data resolution. The strain data are sampled every 18 minutes. We can get slightly better temporal resolution when we stack the records because the samples are staggered relative to the earthquakes. Samples occur 5 and 23 minutes after some earthquakes but 10 and 28 minutes after others. Our stack has nodes at 3, 13, and 23 minutes before and after the earthquakes.

Figure S25 shows the accumulation of strain in the first 40 minutes after the earthquakes. For the two largest-magnitude groups, it seems clear that most of the strain accumulates within the first 3 minutes. There may be some strain in the following 20 minutes, but nowhere near enough the factor of 3 discrepancy between the predicted and observed coseismic strain.

One could still try to explain the large coseismic steps of the larger magnitude groups using early postseismic slip, but that slip would have to accumulate in the first 3 minutes. The required magnitude is not entirely implausible. If moment accumulates logarithmically with time, and the early ($<$ 3-minute) postseismic slip has moment comparable to that accumulated between 20 minutes and 1.5 days, postseismic slip would have to be accumulating logarithmically starting 1 s after the earthquake. Whether postseismic slip starts in earnest within 1 s is unclear, however, as some initial growth and acceleration is expected [*Marone et al.*, 1991; *Perfettini and Avouac*, 2004; *Savage*, 2007; *Amoruso and Crescentini*, 2009]. Indeed, Figure S24 shows that postseismic slip after M 2.7-3.5 earthquakes achieves a logarithmic accumulation only about an hour after the earthquakes.

S9 Alternative Uncertainty Estimates: Inverting Intervals Without Earthquakes

As an alternative approach to determining the uncertainty in our relative moment estimates, we consider portions of the data at non-earthquake times as realizations of the noise. To determine what spurious strain offsets we might obtain, we shift the assumed times of all the earthquakes forward or backward by 50 to 320 days. We then invert the data assuming these incorrect times.

Figure S26 shows histograms of the offsets obtained for 56 different time shifts. These uncertainties are similar to the uncertainties obtained from bootstrapping in Figures 7 and S24.

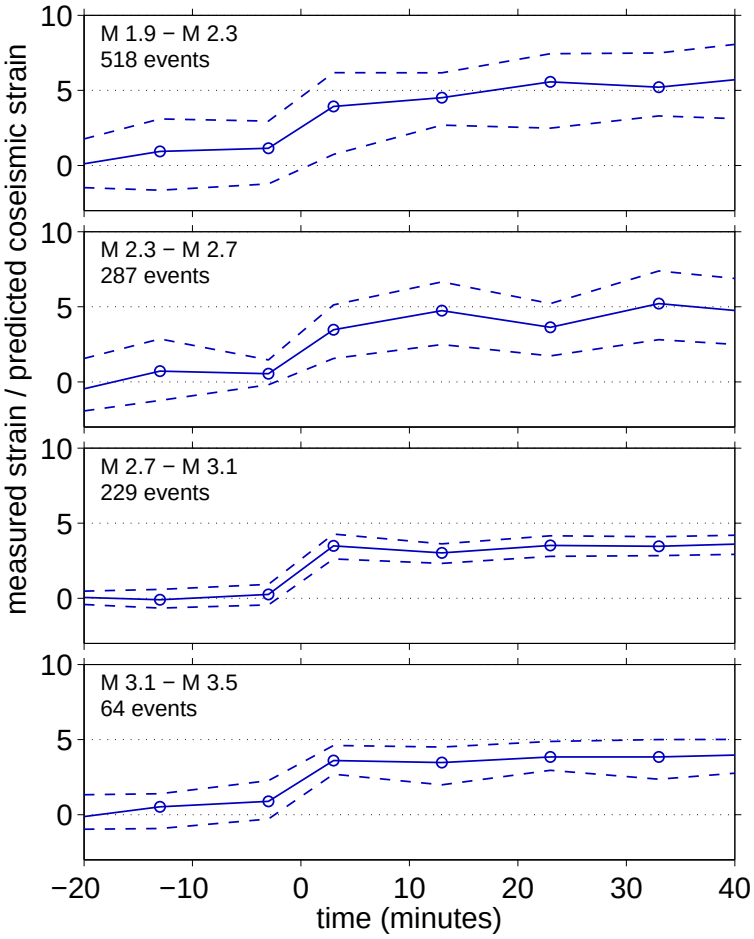

Figure S25. Estimated strain accumulation in the 20 minutes before and 40 minutes after the earthquakes, as in Figure 6. Each panel is for a different magnitude group. For the two larger magnitude groups, it is clear that most of the coseismic strain accumulates within the smallest time interval used—3 minutes.

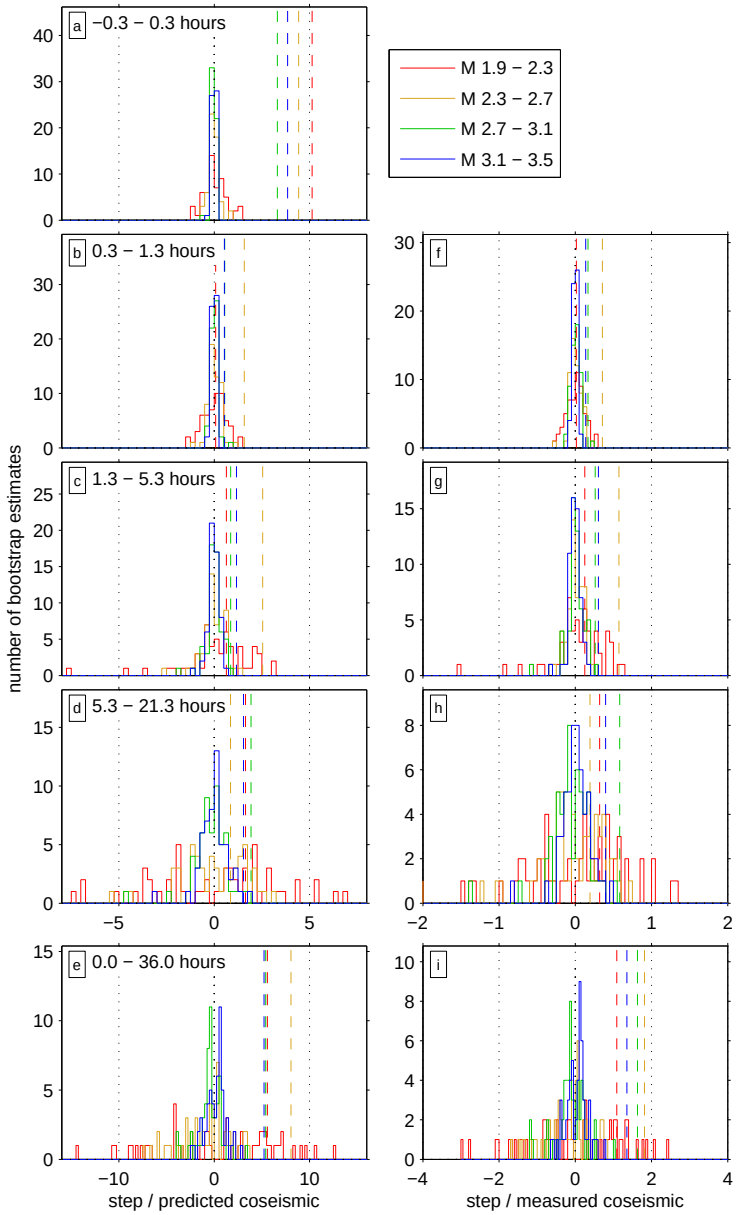

Figure S26. Histograms: distribution of strain offsets obtained by inverting data at times without earthquakes. Vertical dashed lines: best-fitting values obtained from the inversion of earthquake data. The text in the upper left of each panel indicates the time range of the offset for each row. In the first column, the offsets are normalized by the predicted coseismic strain. In the second column, they are normalized by the best-fitting coseismic offsets from the earthquake time series. The coseismic (20-minute, first row) and total (1.5-day, bottom row) offsets are well-resolved. The range of spurious signals obtained from the shifted inversions are similar to the range of errors estimated from bootstrapping (Figure S24).

S10 Comparison With Postseismic Slip After Large Earthquakes

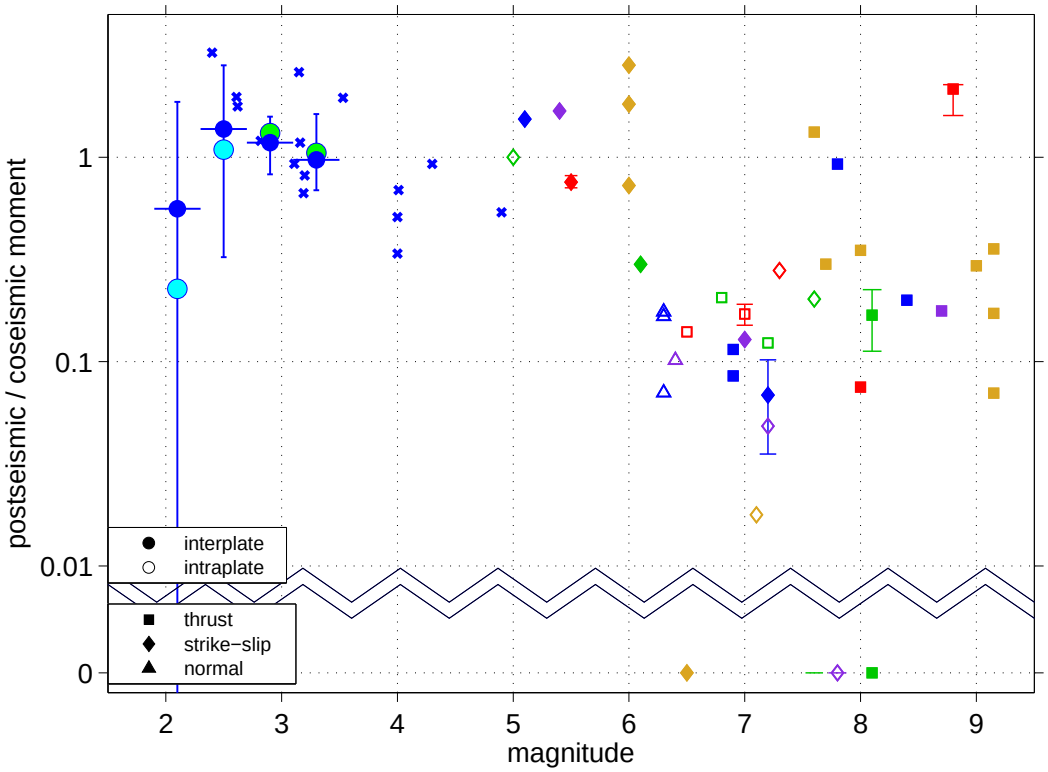

Figure S27. Postseismic moments observed in this study and for some large earthquakes. Moments estimated for $M < 5$ earthquakes are the postseismic moments observed from 20 minutes to 1.5 days after the earthquakes, relative to the coseismic moments. As in Figure 7, circles are for stacked groups, and crosses are for individual earthquakes. Squares plotted for larger earthquakes show the estimated postseismic to coseismic moment ratios estimated a variety of studies. Color differentiates earthquakes, repeating for earthquakes with different magnitudes. Colors are the same for multiple postseismic moments of an individual earthquakes. The observation times vary from days to years among the large earthquakes. Results are taken from *Heki et al.* [1997]; *Savage and Svarc* [1997]; *Segall et al.* [2000]; *Bürgmann et al.* [2001]; *Jacobs et al.* [2002]; *Melbourne et al.* [2002]; *Miura et al.* [2004]; *Hsu et al.* [2006]; *Langbein et al.* [2006]; *Pritchard and Simons* [2006]; *Subarya et al.* [2006]; *Chlieh et al.* [2007]; *Freed* [2007]; *Podgorski et al.* [2007]; *Ryder et al.* [2007]; *Barbot et al.* [2008]; *Furuya and Satyabala* [2008]; *Jónsson* [2008]; *Mahsas et al.* [2008]; *Amoruso and Crescentini* [2009]; *Murray-Moraleda and Simpson* [2009]; *Cheloni et al.* [2010]; *Johanson and Bürgmann* [2010]; *Ryder et al.* [2010]; *Bell et al.* [2012]; *Cetin et al.* [2012]; *D'Agostino et al.* [2012]; *Wen et al.* [2012]; *Lin et al.* [2013]; *Dogan et al.* [2014]; *Gonzalez-Ortega et al.* [2014]; *Taira et al.* [2014]; *Fattahi et al.* [2015].

S11 Likelihood of Large Poroelastic Deformation

We have interpreted the postseismic strain at SJT as the result of afterslip. An alternative explanation, noted in section 7.3, is that the strain results from poroelastic deformation as the pore pressure re-equilibrates. We do not have direct observations confirming or excluding poroelastic deformation. Here we consider the plausibility of such large poroelastic strain given the relevant physical parameters and observations of other signals at SJT.

Pore pressure re-equilibration can happen on two scales: throughout the crust or in near-surface aquifers. We consider each of these below.

S11.1 Crustal-scale diffusion

Crustal-scale poroelastic relaxation has been inferred from geodetic observations after several large earthquakes, including the 1992 M 7.2 Landers, CA earthquake [*Peltzer et al.*, 1996, 1998] and two M 6.5 earthquakes in Iceland in 2000 [*Jónsson et al.*, 2003]. In those cases, pore pressure re-equilibrated over several to tens of kilometers over the course of weeks to years [*Peltzer et al.*, 1996, 1998; *Jónsson et al.*, 2003]. The postseismic strain at SJT accumulates more quickly, over hours to days. However, the length scales near SJT are also shorter: several kilometers rather than several to tens of kilometers. A plausible distance for pore pressure diffusion is often given as $\sqrt{\kappa t}$ [e.g. *Manga and Wang*, 2007] where κ is diffusivity and t is time. Pore pressure diffusion over several km within 1 day would imply a hydraulic diffusivity of order 10 m^2/s. This diffusivity is on the higher end of diffusivities obtained from earthquake triggering [e.g. *Talwani et al.*, 2007; *He and Peltzer*, 2010; *Chen et al.*, 2012]. Thus a 1-day timescale for poroelastic strain accumulation at SJT is plausible.

The magnitude of the observed strain, on the other hand, appears excessively large. For the earthquakes examined here, the observed postseismic strain is equal to or larger than the coseismic strain. At Landers, postseismic displacements are of order 5 cm, just a few percent of the several meters of slip in the mainshock [*Peltzer et al.*, 1996, 1998]. Postseismic displacements were also a few cm in the Iceland earthquakes, again a few percent of the 1 m of coseismic slip [*Jónsson et al.*, 2003; *Pedersen et al.*, 2003].

Physical models also predict small poroelastic deformation. Poroelastic deformation can be modeled by considering two elastic responses to the earthquake: an instantaneous undrained response and a long-term drained response. The two responses can be modeled with a drained

and undrained Poisson's ratio [*Rice and Cleary*, 1976; *Jónsson et al.*, 2003]. In laboratory experiments, the drained and undrained Poisson's ratios are 0.2 to 0.3 and 0.25 to 0.35 for granite and 0.1 to 0.2 and 0.25 to 0.35 for sandstone [*Rice and Cleary*, 1976; *Hart and Wang*, 1995, e.g.]. We compute the expected poroelastic deformation at SJT for a relatively large change in Poisson's ratio of 0.1. We use an undrained Poisson's ratio of 0.3 to estimate the coseismic strain, plotted in the first column of Figure S28. We use a drained Poisson's ratio of 0.2 to estimate the long-term strain, plotted in the second column. The ratio of the long-term to the coseismic strain is plotted in the final column. As in Figure S1, the axes indicate the distance of a hypothetical earthquake from the strainmeter as a fraction of its depth, and the earthquakes included in our analysis are plotted with small circles.

For all of the earthquakes here, the ratio of the predicted long-term ε_{E-N} strain to the coseismic ε_{E-N} strain is between 0.9 and 1.6, and there is only small central region with values larger than 1.2 (Figure S28f). The strain ratio does not approach values of 2 or 2.5, as would be required to match the observed strains. If we further decrease the drained Poisson's ratio to 0.1, the maximum strain ratio reaches 2.2, but only in a small central region that has small predicted strains. These small amplitudes make it appear unlikely that a crustal-scale diffusion of pore pressure can explain the observed postseismic strain.

S11.2 Near-surface diffusion

While large-scale poroelastic deformation is typically small relative to the initial deformation, the local response can be much larger. Near-surface structures can enhance the static response, and changes in material properties or sealing sometimes result from static and dynamic stresses [e.g., *Quilty and Roeloffs*, 1997; *Roeloffs*, 1998; *Chia et al.*, 2001; *Matsumoto et al.*, 2003; *Wang et al.*, 2004; *Manga and Wang*, 2007].

However, if local structures do respond in such a complicated way, they are likely to respond to a variety of applied stresses. Here we look for a local poroelastic response to several signals at SJT.

S11.2.1 No response to large shaking

Water levels in wells sometimes change after earthquakes, even at locations that more than several hundred kilometers from the event. These changes are thought to be a response to dynamic stresses near the well which change the permeability structure, compaction, or seal-

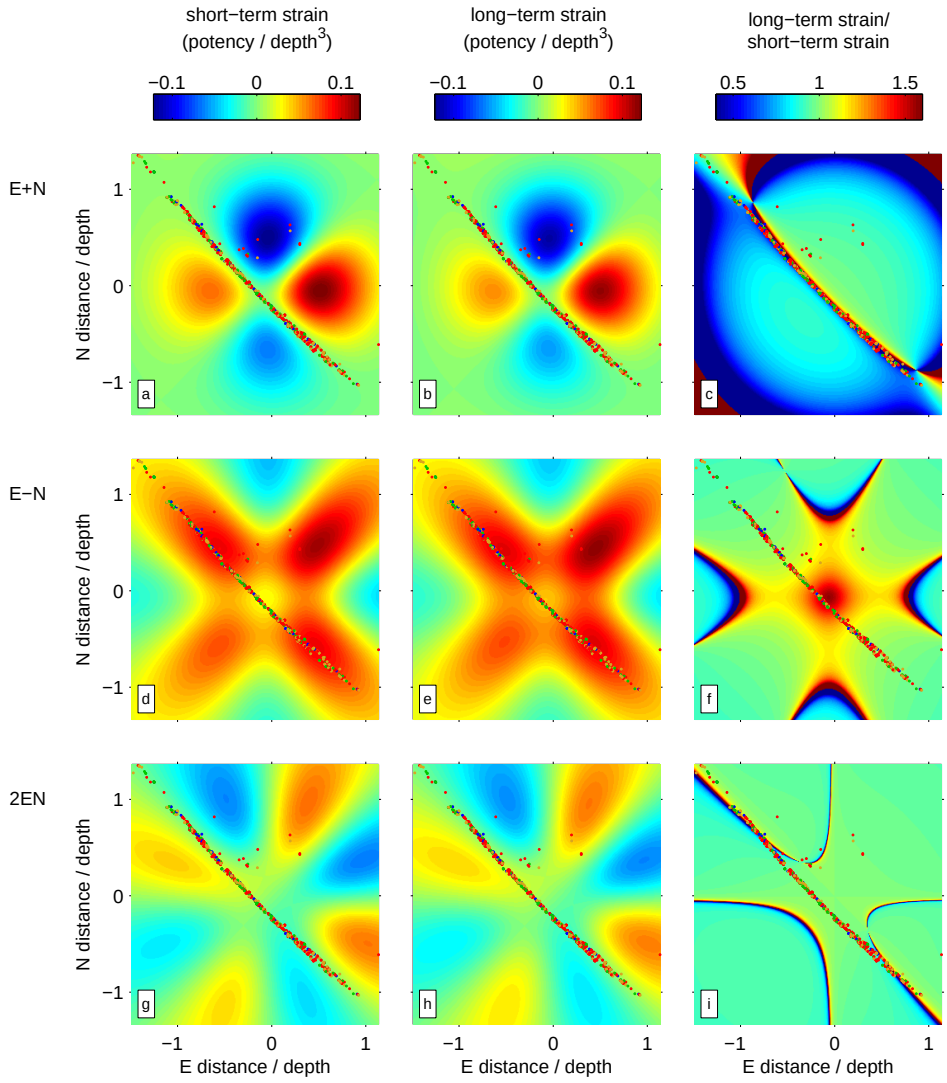

Figure S28. (a) Predicted coseismic strain for ε_{E+N}, assuming a Poisson's ratio of 0.3. As in Figure S1, the axes indicate the strainmeter location relative to the earthquake, and strains are normalized by the earthquake's potency over depth cubed. (b) Predicted long-term strain for ε_{E+N}, assuming a Poisson's ratio of 0.2. (c) Ratio of the predicted long-term strain to the coseismic strain for ε_{E+N}. (d-f) As in a-c, but for ε_{E-N}. (g-i) As in a-c, but for ε_{2EN}. Small colored circles indicate the earthquakes used in our analysis. For most earthquakes of interest, the predicted long-term ε_{E-N} differs from the coseismic strain by only a few to a few tens of percent (panel f).

ing of aquifers [e.g., *Roeloffs*, 1998; *Matsumoto et al.*, 2003]. As a first check of the response to shaking at SJT, we can examine the sign of the accumulated strain. On the ε_{E+N}, and ε_{2EN} components, the sign of the coseismic strain varies with earthquake location. For ε_{E+N}, 4 well-resolved offsets are positive and 8 are negative. For ε_{2EN}, 1 offset is positive and 6 are negative. The sign of the postseismic strain also varies—it usually has the same sign as the coseismic offsets (Figure 7b). In contrast, hydrologic responses to shaking generally have the same sign regardless of the earthquake location [e.g., *Roeloffs*, 1998; *Matsumoto et al.*, 2003]. The consistent sign thus suggests that the observed postseismic strains are more consistent with afterslip.

As a second test, we can consider how the strains change with earthquake distance. The static stress change due to earthquake decays as 1 over distance r^3, while the body wave dynamic stresses at a specified period decays as $1/r^2$ [e.g., *Aki and Richards*, 2002]. In Figure S30 we plot the distances and magnitudes of $M \geq 3$ earthquakes in the NCSN catalog. We calculate M_0/r^3 and M_0/r^2 for each earthquake and exclude earthquakes if these values are larger for another earthquake within 2 days. We then calculate the strain change over 1.5 days starting 30 minutes after each earthquake. Points are colored according to these values. Yellow and red points indicate strain steps that are significant at the 90% level, The three dashed lines indicate lines of constant M_0/r^3, the expected static stress scaling, constant M_0/r^2, the expected dynamic stress scaling on timescales longer than the earthquake, and constant M_0/r, the expected dynamic displacement scaling on timescales longer than the earthquake. The $1/r^3$ scaling better predicts the criteria for significant strain change, suggesting that static stresses, not dynamic stresses, are the primary cause of postseismic strain changes.

The dynamic stress and displacement scalings in Figure S30 assume that the frequency of the shaking that triggers deformation is longer than the earthquake. If shaking on the second-long earthquake timescales is important, we need to consider the earthquake moment rates in our dynamic stress calculations, as discussed in section S3.2. Figure S29 shows the observed postseismic offsets as a function of the predicted static strain scaling (panel a), dynamic strain scaling (panel b), and the dynamic displacement scaling (panel c). Given the scatter, all of these scalings could reasonably match the data.

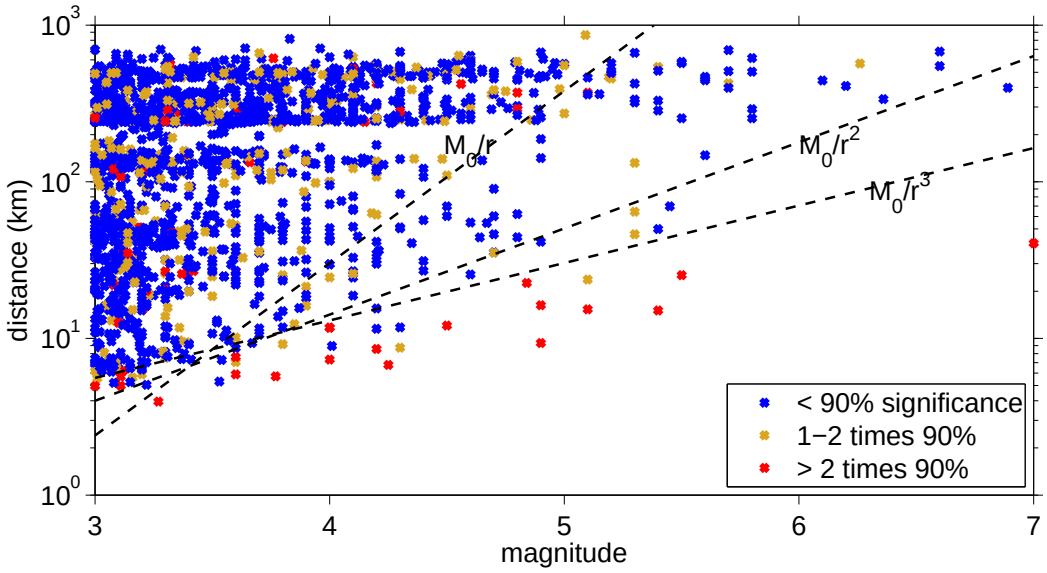

Figure S29. Distance of earthquakes from the strainmeter versus magnitude. Points are colored by the strain change in the 1.5 following the earthquakes, normalized by the 90% significance level. Lines indicate constant values of M_0/r^3, M_0/d^2, and M_0/d, the expected amplitudes of static and dynamic stresses and displacements.

S11.2.2 Small response to atmospheric pressure

One persistently occurring stress change at SJT is the effect of atmospheric pressure. Atmospheric pressure changes are uniform over relatively large regions, and thus produce dominantly vertical strain. Borehole strainmeter records the horizontal components of strain and thus should respond weakly to atmospheric pressure. However, if there were strong anisotropy or heterogeneity near the strainmeter, or if the strain gages are somehow coupled to the vertical strain, atmospheric pressure changes can more strongly affect the recorded strain [*Roeloffs*, 2010; *Hodgkinson et al.*, 2013].

Here we search for a response to atmospheric pressure that may indicate strong heterogeneity and fluid flow. We compare the horizontal strains with 6-hour atmospheric pressure variations from the ECMWF model [*Dee et al.*, 2011], as in section S2. We also compare them with atmospheric pressure variations recorded at nearby PBO strainmeter B058, about 5 km away. This pressure record is shorter—from 2007 to present—but has a higher—30 minute—temporal resolution. The two pressure records match where they overlap. We compare both

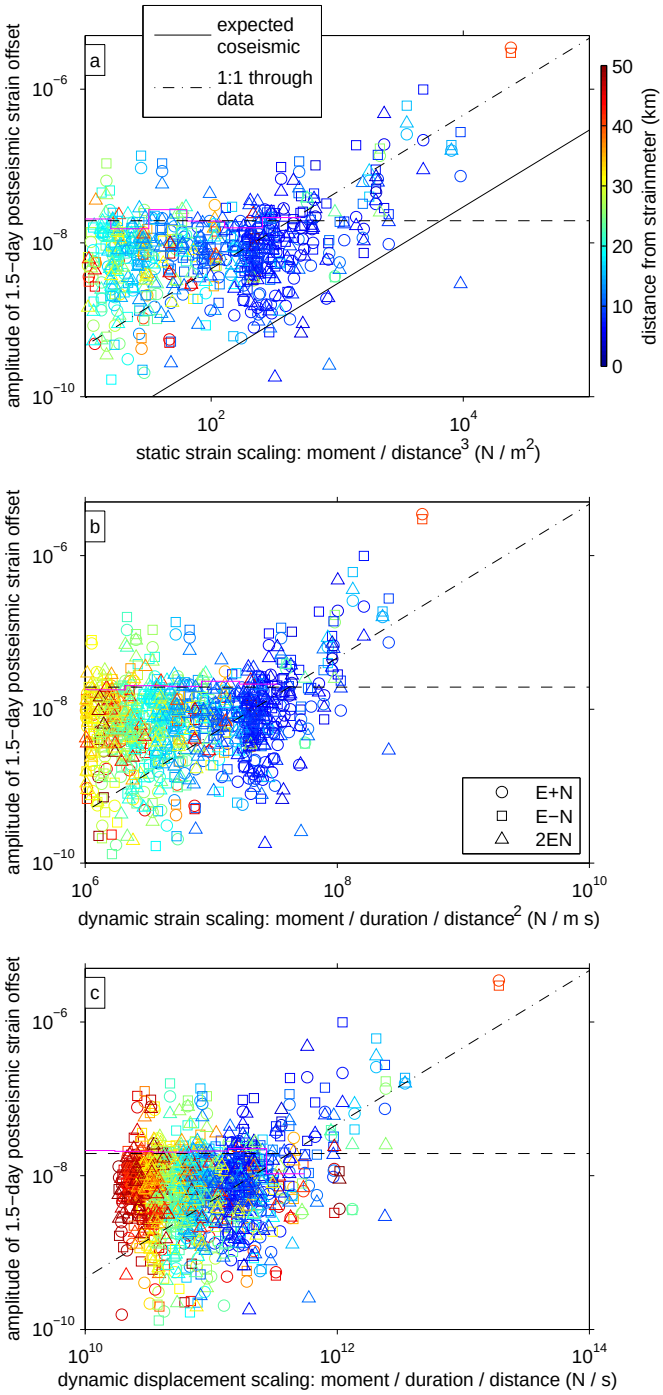

Figure S30. As in Figure S3, but for the postseismic deformation strain offsets, starting 30 minutes after the earthquake. This offset is plotted against the predicted static strain scaling (panel a) and against the dynamic strain (panel b) and displacement (panel c) scalings. These dynamic scalings consider shaking on the mostly sub-second earthquake timescales.

records with the strain between 2007 and 2011, a well recorded interval for both strain and pressure.

When we high-pass filter both records to periods shorter than 5 days, the strain change per barometric pressure change is 5-10 ns / kPa, 2-5 ns / kPa, and 10-20 ns / kPa for the ε_{E+N}, ε_{E-N}, and ε_{2EN} components, respectively. For comparison, the expected vertical strain can be estimated from the atmospheric pressure over the Young's modulus. For a Young's modulus of 50 GPa, the vertical strain could be 20 ns / kPa, 1 to 10 times the horizontal responses. Smaller values for the Young's modulus would predict a larger vertical strain, and these may be more appropriate for near-surface deformation. Indeed, individual strain gages at some PBO strainmeters have barometric responses around 50 ns / kPa, suggesting vertical strains of at least that magnitude [*Hodgkinson et al.*, 2013].

The horizontal strain response suggests a heterogeneous response to atmospheric pressure changes, but it does not necessarily imply poroelastic effects. To look for fluid flow, we consider time and frequency dependence in the barometric response. We find that the ε_{E+N} and ε_{E-N} data are best fit if we the strain is delayed by about 6 and 15 hours from the pressure variations, respectively. In addition, the amplitude of the strain response is reduced by up to 70% if we high-pass filter to periods shorter than 1 or 2 days. The apparently delayed response is consistent with fluid flow re-equilibrating on timescales of 1 day. However, the reduced high-frequency response could also be due to noise or poorly understood signals in the higher-frequency pressure data.

The barometric response at SJT thus allows either possibility: a large-magnitude poroelastic response or no poroelastic response. If the vertical barometric response at SJT is 20 ns / kPa, and if the small strain response at high frequencies results from changes in fluid pressure, the poroelastic response could be comparable to the applied strain. Alternatively, if the vertical barometric response is 50 or 100 ns / kPa, and the apparent reduction in response at high frequencies is actually due to noise or short-wavelength signals in atmospheric pressure, the poroelastic response could be less than 50% of the applied strain, or zero.

The inconclusive poroelastic response at SJT is made more complicated by the fact that the stress tensor induced by atmospheric pressure differs from the stress tensor created by local earthquakes. In the next section we investigate the poroelastic response of shallow creep events, which again have a different combination of stresses.

S11.2.3 Little deformation after creep events

Creep events near SJT occur several times a year on the San Andreas Fault near San Juan Bautista, which reaches the surface about 1.5 km NW of the strainmeter [*Gladwin et al.*, 1994]. Figure S31b shows the strain records associated with one creep event, and Figure S31c shows the creep observed at USGS creepmeter XSJ [*Schulz*, 1989]. *Gladwin et al.* [1994] proposed that most of the slip in these events accumulates at a depth of several hundred meters, over the course of one to two hours. This slip accumulation is reflected in the recorded strain. The rupture then continues upward and produces significant surface creep about 12 hours later, but the moment accumulated during this longer interval is small.

In this study, we are interested in the fact that strain accumulates over 1 to 2 hours and then remains roughly steady. In individual observations, we do not see a day-long poroelastic response to the 1-hour elastic strain. To further confirm the small day-long deformation, we extract a 3-hour and a 1.5-day strain change from 20 creep events. The start time is the leftmost circle in Figure S31b, and the stop times are the sets of circles to the right. The 90% error bars are obtained from 3-hour and 1.5-day strain changes at random times in the 30-year record. In Figure S31a we plot the ratio of the 1.5-day strain change to the 3-hour strain changes.

This ratio clusters around 1. The medians ratios are 1.00, 1.05, and 1.05 for the ε_{E+N}, ε_{E-N}, ε_{2EN} strains, respectively. 90% of the ratios are within 35% of 1, and much of the variation can be explained by noise. A value of 1 falls within the 90% probability range for 75% of the ratios, suggesting that there is some signal after the first 3 hours, but that it is small—of order 1 to 10% of the initial signal. The small signal suggests that the local poroelastic response to stresses associated with creep events is less than about 10% of the elastic strain.

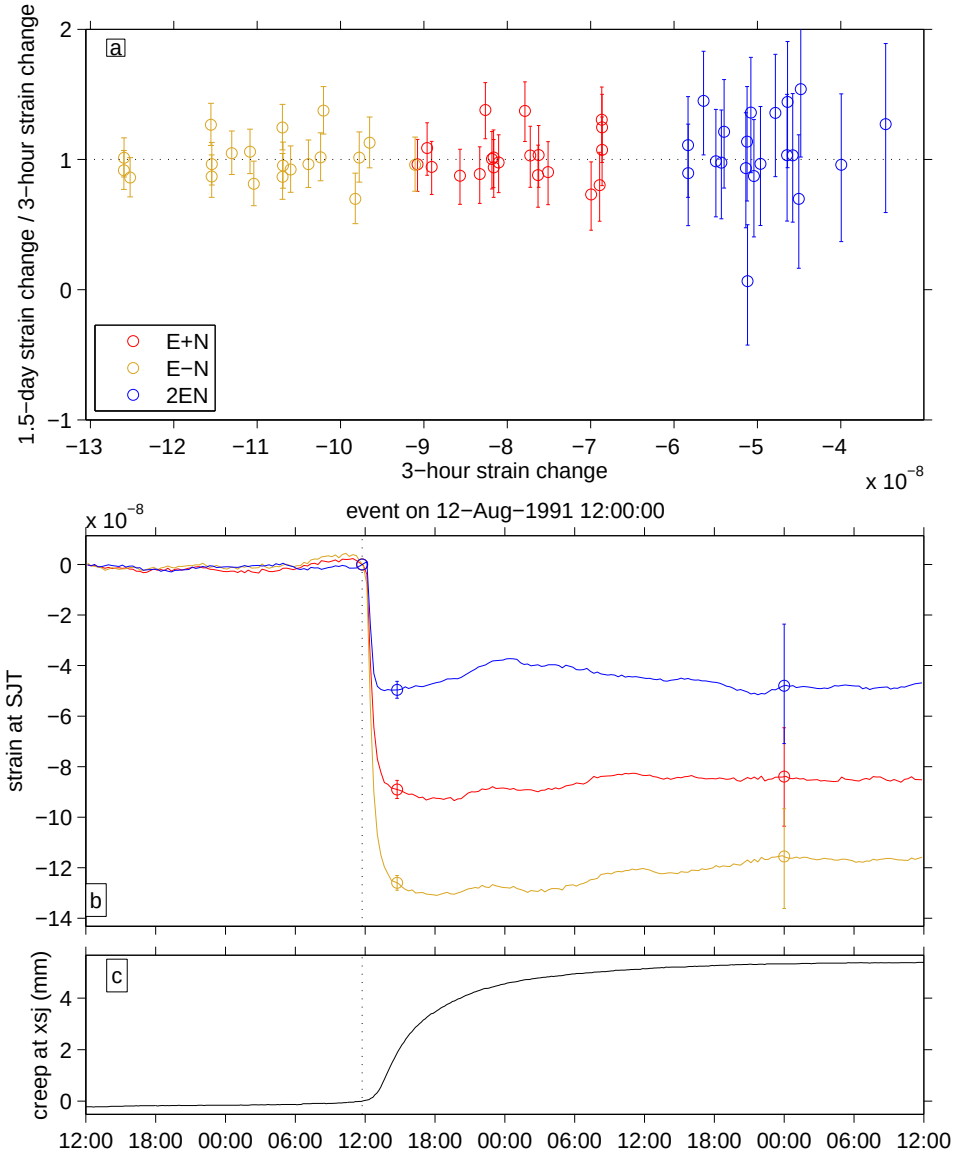

Figure S31. Summary of strain associated with nearby creep events. Panels b and c show the strain and creep associated with one creep event. The strain (panel b) accumulates over just 1-2 hours, while the creep (panel c) often lasts a day. This suggests that the slip event is mostly at depth, with dominant slip over an hour and that the strain does not show a strong poroelastic response to this slip over the following day. Panel a summarizes strain from 20 creep events, showing the ratio of the strain accumulated over 1.5 days to that accumulated over the first 3 hours. The ratio is near one since there is little strain after the first 3 hours. In panels a and b, color indicates the component of strain.